Journal of Volcanology and Geothermal Research 466 (2025) 108407

Contents lists available at ScienceDirect

Journal of Volcanology and Geothermal Research

journal homepage: www.journals.elsevier.com/journal-of-volcanology-and-geothermal-research

Fracture dynamics and topographic controls at Mount Thorbjörn during the Svartsengi 2023–2024 volcanic unrest, Iceland

Maria Hurley [a,b,*], Nicolas Oestreicher [c,d,e], Alina V. Shevchenko [a], Gregory P. De Pascale [f], Magnús T. Gudmundsson [f], Egill Á. Gudnason [g], Gylfi P. Hersir [h], Benjamin F. De Jarnatt [a,b], Alea Joachim [b], Joël Ruch [e], Fabio L. Bonali [i], Thomas R. Walter [a,b]

[a] GFZ Helmholtz Centre for Geosciences, Potsdam, Germany
[b] Institute of Geosciences, University of Potsdam, Potsdam, Germany
[c] Department of Earth Sciences, University of Geneva, Geneva, Switzerland
[d] WSL-Institut für Schnee- und Lawinenforschung SLF, Davos, Switzerland
[e] Climate Change, Extremes and Natural Hazards in Alpine Regions Research Centre CERC, Switzerland
[f] Institute of Earth Sciences, University of Iceland, Reykjavík, Iceland
[g] Iceland GeoSurvey (ÍSOR), Kópavogur, Iceland
[h] Independent researcher, Reykjavík, Iceland
[i] Department of Earth and Environmental Sciences, University of Milan-Bicocca, Milan, Italy

ARTICLE INFO

Keywords:
Fracture-topography interaction
Dyke-induced graben
Drone photogrammetry
Reykjanes Peninsula
Volcano-tectonic unrest

ABSTRACT

Regions with complex topography experience varying degrees of deformation during volcano-tectonic events. Few studies have investigated the relationship between topography and fracturing in detail, and therefore insights into this interplay are limited. In this work, we analysed deformation patterns during the 2023–2024 volcanic unrest on the Reykjanes Peninsula, Iceland, focusing on the dyke-induced graben episode of 10 November 2023. Our study is centred on Mount Thorbjörn, the ~200 m high glaciovolcanic edifice located on the western shoulder of the graben. We collected four drone photogrammetric datasets between 2022 and 2024, covering different phases of the volcanic unrest. By comparing cm-resolution orthophotos and digital elevation models, we identified transtensional reactivation of pre-existing grabens, with normal offsets reaching 80 cm and 20–30 cm of dextral strike-slip. Larger offsets in the south-eastern sector of the mountain suggest tilting in line with the regional deformation trend, although the displacement in the mountain was high compared to lower adjacent regions. Orthophoto comparison revealed ~9 km of new cumulative surface fractures and over 200 sinkholes, with 88 % of the fractures and 59 % of the sinkholes formed during the November 2023 graben event. Statistical analyses indicate a strong topographic influence on fracture development. Fracture density increased with elevation, clustering around local peaks. Our results provide a conceptual model for fracture dynamics in complex topographies during volcanic unrest, where higher elevations are more sensitive to deformation, leading to greater damage.

1. Introduction

Topography and magmatic activity interact in complex ways, as observed in natural and experimental settings. This complexity is particularly evident when magma ascends through the crust in the form of dykes, which are subvertical, planar intrusions of magma representing the most common mode of magma ascent through the crust (Mastin and Pollard, 1988; Segall, 2010). When dykes intrude beneath or near complex topography, they tend to develop inclined or arrested pathways, generate asymmetric graben faults, and experience altered propagation dynamics. Examples of topographic controls on dyke ascent and faulting can be found worldwide, such as in Laki (Iceland), Fogo (Cape Verde), Sierra Negra (Galápagos), Mount Etna (Italy) and La Palma (Spain) (Bonaccorso et al., 2010; Davis et al., 2021; Maccaferri et al., 2017; Trippanera et al., 2015; Walter et al., 2023).

Topography controls the process of dyke ascent towards the surface through the interaction of two key factors: topographic loading and topographic geometry (Gaffney and Damjanac, 2006; Maccaferri et al.,

* Corresponding author at: GFZ Helmholtz Centre for Geosciences, Potsdam, Germany.
E-mail address: maria.hurley@gfz.de (M. Hurley).

https://doi.org/10.1016/j.jvolgeores.2025.108407
Received 7 February 2025; Received in revised form 5 July 2025; Accepted 6 July 2025
Available online 9 July 2025

2014; Pinel and Jaupart, 2000; Tibaldi, 2015). Young volcanic regions typically exhibit significant topographic gradients due to the edifices that form after successive eruptive events. This leads to variable loading conditions; hence, variable lithospheric stress states in volcanic regions, as shown in numerical models (Gaffney and Damjanac, 2006; Pinel and Jaupart, 2004a; Pinel and Jaupart, 2004b), affecting the behaviour of magma pathways towards the surface (Rivalta et al., 2019 and references therein). As a result, the trajectory, orientation and velocity of magma propagation can change (e.g., McGuire and Pullen, 1989). Dykes are typically attracted to topographic loads during their ascent (Dahm, 2000; Maccaferri et al., 2017; Muller et al., 2001; Sigmundsson et al., 2015; Watanabe et al., 2002) and tend to decelerate or even arrest near the load source due to the high confining stresses (Kervyn and Ernst, 2009; Maccaferri et al., 2017; Pinel and Jaupart, 2004b), favouring magma storage at depth when loads are excessive. Depending on the geometry of the load, dykes can sometimes bend and propagate laterally until they extrude at lower elevations (Gaffney and Damjanac, 2006).

With respect to magma-induced deformation from an expanding source at depth, Interferometric Synthetic Aperture Radar (InSAR) observations indicate that deformation patterns vary significantly in areas with topographic gradients (Cayol and Cornet, 1998; Williams and Wadge, 1998; Williams and Wadge, 2000). Subsequent studies using tilt data (Beauducel and Carbone, 2015) and Global Navigation Satellite System (GNSS) data (Hickey et al., 2024) have built on these findings and demonstrated that three-dimensional models are more accurate than traditional analytical models for interpreting magmatic activity at depth.

For dyke intrusions, analytical models have shown that they cause surface subsidence above the dyke tip and uplift towards the sides due to stress field changes (Pollard et al., 1983; Rubin and Pollard, 1988). Eventually, the deformation becomes brittle, forming two inward-facing normal faults that bound a graben (Mastin and Pollard, 1988; Pollard et al., 1983; Wright et al., 2006). In areas with topographic gradients, the graben-bounding faults typically converge and diverge with changes in elevation, creating complex fault geometries (Acocella and Neri, 2009; Bonali et al., 2024; Trippanera et al., 2015; Trippanera et al., 2019; Walter et al., 2023; Wooller et al., 2009). Studies have linked eruption locations to topography-induced bending of the faults forming the graben, such as in Laki, Iceland (Trippanera et al., 2015) and on Tajogaite-Cumbre Vieja volcano, La Palma (Walter et al., 2023). This relationship highlights the importance of understanding the interaction between topography and faulting, which may have important implications for eruption forecasting.

In non-magmatic settings, topography-induced stresses may exceed tectonic stresses in proximity to topographic landforms within the uppermost crust (Tibaldi, 1998), leading to a first-order control of topography in surface fracturing. Mathematical approaches and field observations have shown that topography favours rock fracturing processes within regional (e.g., McNutt, 1980; Ricard et al., 1984) and local scale topographic changes (McTigue and Mei, 1981; Tibaldi, 1998). The resulting fracture distribution is therefore closely related to landform geometry (Miller and Dunne, 1996; Tibaldi, 1998). Other fracture complexities such as in the geometry (strike and dip), kinematics (rake and slip), and segmentation have also been attributed to topographic effects (Koons and Kirby, 2007; Tibaldi, 1998; Upton et al., 2017).

However, as many volcanoes worldwide are located close to tectonic boundaries, interactions between regional tectonics, topography and local volcanic deformation need to be considered.

At divergent plate boundaries, crustal extension can occur through tectonic or magmatic induced faulting, with their relative contributions depending on the spreading rates and magma supply (Sigmundsson, 2006). In mature rift zones such as in Iceland, magma availability is generally high, and rifting is largely accommodated through short-lived diking episodes that release tectonic stresses accumulated during longer inter-rifting periods (Acocella, 2021 and references therein; Acocella and Trippanera, 2016). Regional tectonic stress is still a key factor, as it modulates and contributes to the temporal and spatial distribution of the dyke emplacement (Acocella, 2021; Buck et al., 2006). In oblique rift systems like the Reykjanes Peninsula, tectonic stress is particularly relevant, as the higher shear-to-extension ratio, combined with a lower magma supply, may induce longer inter-rifting periods of up to 1000 years (Sæmundsson et al., 2020; Sigmundsson, 2006).

In October 2023, a new phase of volcanic unrest began in the Svartsengi-Eldvörp Volcanic System (hereafter referred to as Svartsengi) on the Reykjanes Peninsula in southwest Iceland, involving significant dyke-induced surface deformation (De Pascale et al., 2024; Sigmundsson et al., 2024). This study investigates the interaction between topography and dyke-induced deformation. The region presents a relatively flat landscape dominated by subaerial lavas, where older subglacial volcanic landforms form local topographic highs (Pedersen and Grosse, 2014; Sæmundsson et al., 2016). The interplay between extended deformation, faulting and the topographic features of the region make this site ideal for investigating topographic controls on deformation. Using drone-derived data, we conducted a detailed analysis of fracture formation and evolution at Mount Thorbjörn, a flat-topped mountain largely affected by such events. Our results present a preliminary model of topographic effects on faulting during volcano-tectonic unrest.

2. Study area

2.1. Tectonic setting

The Reykjanes Peninsula oblique rift, located on the southwest tip of Iceland (Fig. 1), is an onshore section of the Mid-Atlantic Oceanic Rift that is oriented approximately 30° counterclockwise with respect to the spreading direction (DeMets et al., 2010). This high obliquity results in a combination of extensional and strike-slip motion, leading to a complex fault network with high seismic activity and sporadic (~800–1000 years

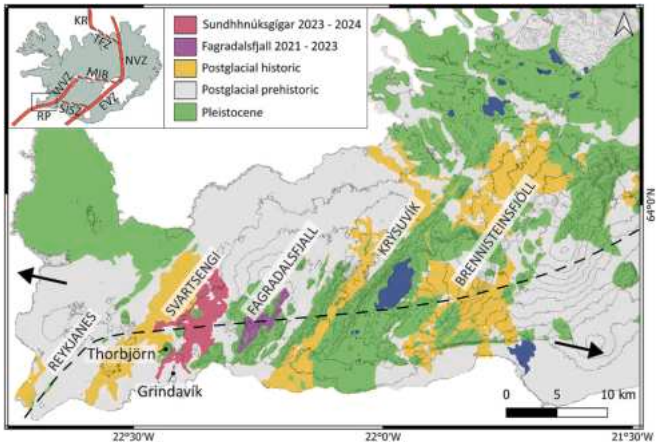

Fig. 1. Geology of the Reykjanes Peninsula oblique rift, showing eruptive units by colour after Sæmundsson et al. (2016). The oldest outcrops (green) are Pleistocene glaciovolcanic units, including Mount Thorbjörn. Postglacial lavas are prehistoric (white) or historic (yellow). The most recent eruptive products (in Fagradalsfjall and Svartsengi) are shown in purple and pink, respectively, and include eruptions up until November 2024, mapped using orthophotos provided via the Icelandic National Land Survey's Web Map Service (WMS) (https://gis.lmi.is/mapcache/reykjaneseldar/web-mercator/wms). Water bodies are shown in blue. The black dashed line marks the plate boundary; arrows indicate plate movements, according to DeMets et al. (2010). En-échelon volcanic systems are indicated. The inset map of Iceland shows the plate boundaries, including active rifts (red lines) and fracture zones (red dashed lines). RP: Reykjanes Peninsula oblique rift; SISZ: South Iceland Seismic Zone; WVZ: Western Volcanic Zone; MIB: Mid Iceland Belt, EVZ: Eastern Volcanic Zone; NVZ: Northern Volcanic Zone, TFZ: Tjörnes Fracture Zone; KR: Kolbeinsey Ridge. (For interpretation of the references to colour in this figure legend, the reader is referred to the web version of this article.)

between episodes) but long-lived magmatic episodes (Einarsson, 1991; Sæmundsson et al., 2020).

A series of N*E*-striking eruptive fissure swarms forming prominent ridges, crater rows, and glaciovolcanic edifices constitute the main topographic features of the Reykjanes Peninsula (Clifton and Schlische, 2003) (Fig. 1). They are spatially related to non-eruptive tensile fractures and normal faults, which may have resulted from the same volcano-tectonic episodes as the fissure swarms (i.e., dyke intrusions). Arranged in a right-stepping en-échelon pattern, they define the volcanic systems of Reykjanes, Svartsengi-Eldvörp, Fagradalsfjall, Krýsuvík and Brennisteinsfjöll from west to east (Sæmundsson et al., 2020) (Fig. 1), where magmatism is fissural without a central volcano (Walker, 1995). All volcanic systems except Fagradalsfjall host a known high-temperature geothermal field. During amagmatic periods, tectonic movement occurs predominantly along right-lateral strike-slip faults striking ~N-S (and minor left-lateral ~E-W faults), producing the most destructive earthquakes in the area (Árnadóttir et al., 2004; Einarsson, 2008; Keiding et al., 2009).

A detailed description of the structure on the Reykjanes Peninsula was conducted by Clifton and Kattenhorn (2006) based on optical aerial imagery, later refined (Ducrocq et al., 2024; Sæmundsson et al., 2016). Maps revealed populations of N-S, N30–45°E and N45–60°E striking structures, consistent with higher resolution analyses in localised sectors across the Reykjanes Peninsula (Fig. 1) (Bufféral et al., 2023; Einarsson et al., 2020; Hjartardóttir et al., 2023). The structural architecture of the Reykjanes Peninsula exhibits complexities that differ slightly from model-based predictions based on rift obliquity, suggesting that external controls, like spatio-temporal variations, may occur (Clifton and Kattenhorn, 2006).

Postglacial volcanic activity has shaped most of the Reykjanes Peninsula, starting as small picritic and large basaltic shields, later interlayered with fissure eruptions (Sæmundsson et al., 2016). Before the recent volcanic activity, the last eruptive cycle across the Reykjanes Peninsula started in the 8th century and ended ~800 years ago (Sæmundsson et al., 2020). Magma storage depths for this cycle have been estimated at 7–10 km beneath Reykjanes, Svartsengi and Krýsuvík based on independent clinopyroxene-melt and melt-based barometry, and eruptive dynamics included rapid magma ascent and prolonged eruptions (Caracciolo et al., 2023).

Some of the oldest Reykjanes Peninsula outcrops correspond to glaciovolcanic edifices formed during Pleistocene glaciations (Sæmundsson et al., 2016) that remain uncovered by younger lava flows due to their prominent relief. Glaciovolcanic landforms present diagnostic morphologies and lithofacies that reflect direct interaction between magma and ice. They can be flat-topped, conical, linear or complex, depending on the conditions during eruption (Russell et al., 2014). Lithofacies found on glaciovolcanic edifices include pillow lavas and breccias, tephra (tuffs and hyaloclastites) and subaerial lavas. Their relative proportions provide genetic information, such as eruption styles, magma composition, and magma-meltwater interaction (Russell et al., 2014). Mount Thorbjörn, within the Svartsengi Volcanic System (Fig. 1), formed in the Early Brunhes (i.e., 780 ka) geomagnetic epoch (Sæmundsson et al., 2016). It has been classified as a pillow-dominated flat-topped, heavily faulted tuya (Pedersen and Grosse, 2014), although important ambiguities exist regarding glaciovolcanic edifice classifications (Pedersen et al., 2020 and references therein), which is why we will refer to it from here on as a glaciovolcanic edifice.

2.2. Volcanic unrest at Svartsengi

An intensification of a new volcano-tectonic episode on the Reykjanes Peninsula was signalled in 2020, associated with the inflation of a magma reservoir beneath Svartsengi (Flóvenz et al., 2022). Eruptions in 2021–2023 occurred further east at Fagradalsfjall (Fig. 1), marking the onset of the new magmatic cycle, but remained linked to an inflation source and associated with upflow of magma from depth (Greenfield et al., 2022; Troll et al., 2024). The eruptions were closely monitored by seismic and various geodetic methods, providing an opportunity to test and improve pre- and *syn*-eruptive hazard predictions (Barsotti et al., 2023). A new phase of volcanic unrest on the Reykjanes Peninsula began in October 2023, centred on Svartsengi. Deep magma accumulation produced sustained surface uplift rates centred northwest of Mount Thorbjörn, followed by the most severe subsidence episode on 10 November 2023 (De Pascale et al., 2024; Sigmundsson et al., 2024). A ~15 km long dyke intrusion caused the observed subsidence, which propagated from the Sundhnúkar crater row to both the northeast and southwest, extending beneath the town of Grindavík and offshore (Sigmundsson et al., 2024). Several normal faults and fractures developed rapidly in the region, forming two grabens separated by a horst and resulting in surface subsidence of over 1 m (De Pascale et al., 2024). Widespread surface fractures had formed or had been reactivated in the region between December 2019 and March 2021 (Ducrocq et al., 2024), but they produced much smaller (<0.015 m) displacements.

The large earthquakes and related fracture activity in the region were particularly destructive to nearby infrastructure, affecting the town of Grindavík, which was evacuated on 10 November 2023. Subsequent tectonics and dyke intrusions (e.g., De Pascale et al., 2024; Sigmundsson et al., 2024) also led to enhanced graben formation and regional extension and subsidence, although smaller in magnitude. This time, magma reached the surface, resulting in a series of eruptions that began in December 2023 and are still ongoing (Fig. S.1, 1).

Our study includes four datasets from July 2022 to August 2024, thus covering the November 2023 graben episode and the first five eruptions and related grabens. These eruptions started on 18 December 2023, 14 January, 8 February, 16 March and 29 May 2024 (Fig. S.1). The first three eruptions lasted between one and three days, while the fourth and fifth eruptions were significantly longer, lasting 54 and 24 days, respectively. The fifth eruption produced about 45 million m^3 of erupted material, the largest volume extruded up to that point (IMO, 2024).

3. Data acquisition and processing

We used satellite remote sensing data to get a regional overview of the deformation in Svartsengi related to the November 2023 graben event and to identify the main deformation trend. For a more detailed analysis of the deformation on Mount Thorbjörn, we carried out field surveys and repeated drone flights, providing high-resolution datasets for temporal monitoring of changes. We analysed and post-processed the drone imagery using a GIS interface, and tracked changes manually and using semi-automated techniques. Finally, we performed statistical analyses to identify trends in the deformation and relate them to potential controlling factors. This workflow provided a comprehensive view of faulting dynamics on the mountain. All data and products (shapefiles, digital elevation models and orthophotos) are available in Hurley et al. (2025).

3.1. InSAR data

To analyse the effects of the 10 November 2023 dyke intrusion event on the Reykjanes Peninsula, we created a high-resolution interferogram using a pair of StripMap Synthetic Aperture Radar (SAR) images acquired by the TerraSAR-X (TSX) satellite (German Aerospace Center) on 9 November 2023 and 20 November 2023. The images were acquired in a descending orbit (track 110) with a perpendicular baseline of 189 m, covering the western part of the Reykjanes Peninsula. X-band radar images allow for high spatial resolution interferograms and are ideal for analysing fracture movements (e.g., Ducrocq et al., 2024). We processed the images using SNAP (ESA Sentinel Application Platform vs. 10.0). We extracted the topographic phase using a 2 m × 2 m digital elevation model (DEM) (2016 ÍslandsDEM, from the National Land Survey of Iceland, available at https://atlas.lmi.is), and the differential InSAR was then multi-looked (5 and 4 range and azimuth looks, respectively,

resulting in a ~8 m × ~8 m pixel size) and filtered using the Goldstein phase filter operator with an adaptive filter exponent of α = 0.8 (Goldstein and Werner, 1998). This process resulted in a wrapped interferogram that allowed us to visualise the surface deformation on the western Reykjanes Peninsula caused by the intrusion. Following Ducrocq et al. (2024), we used the wrapped interferogram to map visible discontinuities in the fringes that may represent surface fracture movement during the analysis period.

3.2. Structural field measurements

Between 24 and 25 April 2024, we monitored fresh fractures and sinkholes on the surface of Mount Thorbjörn. We carried out photographic documentation and in-situ measurements using GPS and a compass, including strike, vertical, and horizontal shear displacements and tensile displacement offsets on some selected outcrops. Field measurements of surface fractures gave insights into the kinematics associated with the deformation events occurring on Mount Thorbjörn and provided essential validation of the remote sensing observations.

3.3. Drone surveys

We used data collected on (1) 23 July 2022, more than a year before the start of the volcanic unrest episode at Svartsengi, then on (2) 18 November 2023, shortly after the first dyke-induced graben had formed, and on (3) 25 April and (4) 20 August 2024, during and between eruptive episodes, respectively. Table A1 provides details of the parameters for each drone flight and data processing. We used three types of drones: a DJI Phantom 4 RTK drone, a DJI Matrice 30T RTK drone, and a WingtraOne PPK fixed-wing drone. The DJI Phantom 4 RTK is a quadcopter equipped with a 1“ CMOS and 20 MPixel optical camera, a single-frequency GPS+GLONASS+Galileo receiver, and a dual-frequency L1/L2 GNSS receiver connected to a base station (located near the drone’s launch site). This allows Real Time Kinematics (RTK) corrections to be made to the GPS data received by the drone, resulting in cm-level accuracy of the drone’s position. The DJI Matrice 30T RTK is also a quadcopter that captures images with a wide-angle camera, a 1/2” CMOS, and a 12-megapixel optical sensor. The drone also has a GNSS receiver that allows for RTK corrections.

The WingtraOne Gen II is a VTOL (Vertical Take-Off and Landing) drone with a 61-megapixel Sony Alpha 7 Mark IV camera. The drone carries a built-in multi-frequency (L1-L2 included) Post Processing Kinematics (PPK) GNSS antenna. PPK, similar to RTK, is a method to correct image geo-tagging, in this case after the flight, using correction data acquired from a fixed GNSS base station on the ground. It has similarly been used in Iceland by Panza et al. (2024). The advantages of using the fixed-wing WingtraOne over quadcopters include larger coverage areas due to the high speeds achieved and the high-resolution of the camera, which allows it to fly higher than other drones while ensuring the same or better Ground Sampling Distance (GSD). Other advantages include the 10 km bidirectional radio link between the drone and the remote control in direct line of sight (without obstacles), and the 50 km range and 50 min autonomy, which is beneficial for large-scale surveys. The autonomy is important for terrain-following flights in areas with significant topographic gradients, such as Mount Thorbjörn, where obstacles can interfere with the radio link. This terrain-following capability ensures a more consistent Ground Sampling Distance (GSD) over uneven terrain. However, their higher sensitivity to bad weather conditions makes them ideal for combination with quadcopters, as the strengths of each type complement each other.

Surveys (1), (2) and (3) were carried out at a constant height of ~120 m above the mountain summit. We surveyed (4) following the terrain at an altitude of ~150 m above the ground. All surveys have 70 % lateral and 80 % frontal image overlap.

We manually checked the quality of each drone survey to keep only high-quality images. Data processing involved applying a Structure-from-Motion (SfM) technique (Westoby et al., 2012) to the overlapping images, using the Agisoft Metashape (vs. 2.0) software package. The processing includes the following steps: (1) Alignment of the acquired images to create a sparse point cloud, (2) Generation of a dense point cloud, (3) Reconstruction of a 3D mesh, and (4) Texture application to produce a realistic model. These steps resulted in the generation of the high-resolution DEMs and orthophotos, which provide detailed representations of the study area. These final products allowed for the analysis of topographic evolution and deformation through quantitative geospatial analysis techniques.

4. Geospatial analysis

The results of the drone imagery processing include orthophotos and DEMs, which we analysed using a GIS interface (QGIS vs. 3.34), focusing on the analysis of changes.

4.1. Manual Tracking of Changes (MTC)

We systematically compared the successive high-resolution drone orthophotos to identify changes in the landscape, providing a broad and comprehensive view of the entire area, including sectors that are difficult to access by foot. For the comparisons, we used the first dataset as the reference and defined synthetic Ground Control Points (GCPs) to align the remaining datasets. We identified several new fractures and associated sinkholes, which we mapped distinguishing the dataset in which they became visible. This way, we created a temporal cumulative map of the recent surface-expressed fractures and sinkholes in the area.

4.2. Semi-automated Change Detection Techniques (SaCDT)

We applied semi-automated change detection techniques to our dataset, including DEM of difference (DoD) and Digital Image Correlation (DIC). Combined, these techniques allow for a thorough deformation analysis. While DoD is applicable to quantify vertical surface changes by comparing pre- and post-event DEMs, DIC provides insights into the horizontal displacements using pre- and post-event orthophotos. These methods are commonly applied for a wide range of geomorphic change detection purposes (e.g., Williams, 2012 and references therein) and for quantifying fault movements (e.g., Scott et al., 2020).

4.2.1. DEM of Difference (DoD)

We generated the DoD maps by subtracting a DEM from another DEM previously acquired using the QGIS raster calculator. We focused only on the November 2023 dyke intrusion episode, as the magnitude of this event was the only one that allowed a good sensitivity of the method. For this, we used the DEMs acquired in July 2022 and November 2023. We began by improving the vertical accuracy of the DoD by using the GNSS station THOB, which is located at the mountain summit, as a vertical reference. Fixed GNSS stations typically provide vertical precision of between 1.5 and 4 mm (Steigenberger et al., 2012), making them valuable reference points for correcting vertical biases in DEMs. In contrast, InSAR measurements provide a dense spatial dataset but are often limited by factors such as large displacements, athmospheric conditions and steep terrain, all of which are present in our study area (Hanssen, 2001). GNSS data have been used to correct InSAR-derived deformation measurements (Yan et al., 2024) and to reference DEMs (Wessel et al., 2018). In this study, we therefore used GNSS station data to reference the DoD, ensuring a more accurate estimation of the vertical displacement. We first identified the position of the station’s antenna in the DEMs, selecting a nearby pixel to avoid potential artifacts from the antenna structure. Then, we compared the vertical displacement given by the DoD at that pixel and the GNSS-measured vertical displacement between the exact two dates when the DEMs were acquired (see supplementary Fig. S.2 for GNSS station data). The difference between the two values (1.2 m) was interpreted as a systematic

vertical bias in the DoD and subtracted from the entire DoD raster using the QGIS raster calculator.

As the mountain has moved both downwards and westwards during the period covered by the DoD (De Pascale et al., 2024; Sigmundsson et al., 2024), the pixel values observed on the DoD are apparent downwards movements as they include displacements due to the westward shift of the mountain. Therefore, after applying the vertical bias correction, we generated DoD profiles that were adjusted using trigonometric levelling to correct for this effect and better approximate the true downward displacement. We estimated the horizontal shift of the mountain by averaging the pixel offset between the July 2022 and November 2023 orthophotos along the direction of the transect. Then, using the slope values along the profile derived from the 2022 DEM, we obtained a corrected vertical displacement value using the following relationship:

$$CVD = DoD - (H \times \tan(\alpha))$$

CVD is the corrected vertical displacement in metres; *DoD* is the original dataset derived directly from the DEM subtraction in metres; *H* is the estimated horizontal displacement in metres and α is the slope angle.

4.2.2. Digital Image Correlation (DIC)

2D DIC is an optical-numerical method used to detect and quantify displacements in an area of interest by comparing two successively acquired images. The method compares co-registered digital images using specific algorithms (here, cross-correlation) and interprets any changes in the patterns between sub-windows as displacements. We applied this technique to the drone orthophotos to analyse horizontal fault displacement over time on the mountain surface.

In recent years, DIC applied to remotely sensed products has proven to be a successful tool for monitoring surface displacement, complementing more widely used ones like InSAR in a wide range of applications, including deforming volcanoes (Le Corvec and Walter, 2009; Walter, 2011; Zorn et al., 2020). We used the LaVision Davis software (vs. 10.0.05), which produces displacement and strain maps in X and Y directions for areas of interest, initially defined by the user by masking the photo sequence and defining a reference. Similar to the DoD, we focused only on the November 2023 dyke intrusion episode. For this, we used the July 2022 and April 2024 orthophotos, as these proved to be the most effective pair for characterising and quantifying the horizontal displacements along fractures due to the November episode, probably due to similar lighting and weather conditions during the acquisition.

4.3. Statistical analyses

We used statistics for correlation analyses between the new surface fractures and the pre-existing mountain morphology, including topography and pre-existing fractures. For all analyses, we used a map rotated 23° counterclockwise to align the main orientation of the pre-existing fractures with the vertical axis. Fracture segments were divided into 1 m sections to ensure that statistical analyses were independent of fracture length. The map was further subdivided into 25 subsections of the DEM along the Y axis, each 60 m high, for different analytical purposes.

To assess topographic controls, we examined the density and orientation of the new fractures and compared them to the elevation and slope of the surface. To test the reactivation of pre-existing fractures, we analysed the spatial distribution of the new surface fractures relative to the older ones. For this, we calculated fracture density plots with a bin size of 10 m in the horizontal direction for each of the 25 subsections, each 60 m high. These density plots were then stacked vertically to generate a 2D map, which was used to examine the spatial relationship between the new and reactivated fractures.

We conducted the statistical analyses in Python and used geospatial libraries (Geopandas, Rasterio, Shapely) to manipulate GIS shapefiles (previously created and manipulated using QGIS). For data visualisation we used the Matplotlib, Seaborn, SciPy and Windrose libraries.

4.4. Uncertainties in fracture analyses

We estimated fracture detection uncertainties for both manual and semi-automated approaches (DIC, DoD). For manual fracture detection, uncertainty is primarily influenced by the resolution of the orthophotos, with the minimum detectable structure being a few pixels in length (from 6 to 10 cm in our orthophotos) and at least one pixel in width. For the DIC, the uncertainty was estimated by aligning the two orthophotos using one reference point in a 30 m × 30 m area northwest of the mountain assumed to be stable. Within this area, the application of DIC led to displacements in the X direction ranging from −20 cm to 40 cm (standard deviation: 7 cm), interpreted as white noise. Displacements in the Y direction ranged from −50 cm to 20 cm, with a standard deviation of 5 cm.

Similarly, for the DoD method, we co-registered both DEMs using a reference point located in the same stable area and calculated the DoD. Zonal statistics were calculated using QGIS, considering a circular polygon of 30 m diameter centred on the reference point. The vertical displacement values here ranged between −50 cm and 50 cm, with a standard deviation of 10 cm, which we consider the method's random error.

Therefore, displacements equal to or smaller than the standard deviation values (i.e., ≤7 cm for DIC and ≤ 10 cm for DoD) are considered to be within the noise level, and hence are not considered reliable for our analysis.

5. Results

5.1. Regional context inferred from InSAR data

The dyke-induced graben produces coherence values that reveal a spatial pattern and allow to track intense NNE-SSW trending surface displacement. Coherence is significantly low on both sides of the graben, indicating strong deformation, and remains relatively high in the central part of the graben (Fig. 2A). North and south of Mount Thorbjörn, at comparable distances from the graben centre, the coherence is sufficient to identify fracture movements, which were active during the period considered (Fig. 2C, E). In contrast, Fig. 2D shows a close-up of the interferogram at Mount Thorbjörn, where the lack of coherence makes it impossible to observe and track fault activity. From the fringe offsets identified in the interferogram (Fig. 2B), we manually mapped active fractures for the analysis period. Within the area covered by the interferogram, we identified a cumulative length of ~200 km of active fractures. Of this, ~150 km had already been active between December 2019 and March 2021, as documented by Ducrocq et al. (2024). The mapped faults occur up to ~13 km from the dyke intrusion, highlighting that the event was regional in scale, and increased the cumulative length of known faults by 25 %. Applying this methodology to long-term datasets covering the period prior to 2020 would enable distinguishing fault activity associated with purely tectonic processes (before 2020) from those related to magmatic episodes (after 2020), providing valuable insights into the long-debated magmatic and tectonic stresses interaction. Fig. 2C and E show detailed views of the interferogram and respective mapped fractures, focusing on the regions north and southwest of Mount Thorbjörn, respectively. Based on optical imagery observations, many of the mapped discontinuities correspond to pre-existing structures, as previously pointed out by Ducrocq et al. (2024).

5.2. Local fault dynamics at Mount Thorbjörn

5.2.1. Global description of Mount Thorbjörn from drone data

Structure-from-Motion processing of the drone optical images acquired over Mount Thorbjörn allowed us to generate one high-resolution DEM and one orthophoto for each survey. Together, they provide a

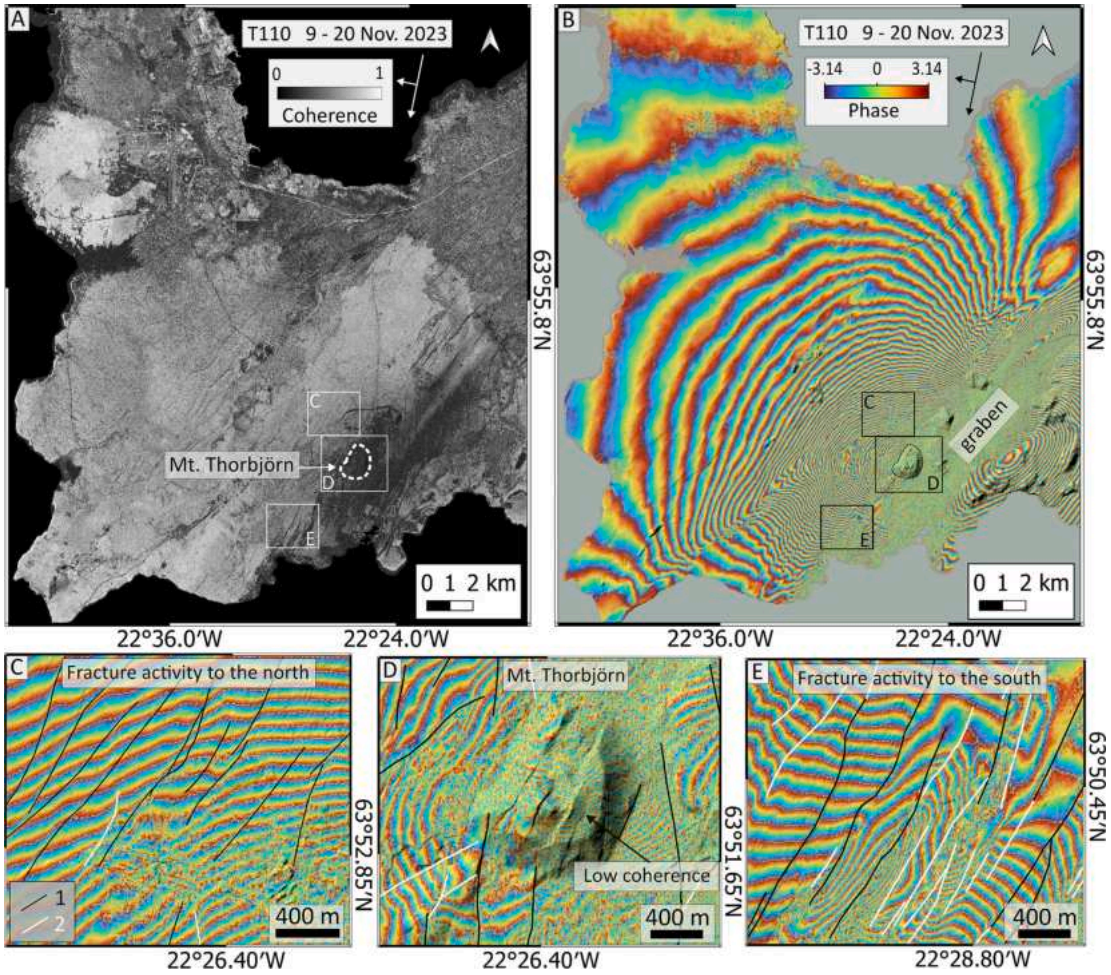

Fig. 2. (A) InSAR coherence map from two TerraSAR-X radar images (9 and 20 November 2023, descending track 110) of the western Reykjanes Peninsula. Dark colors indicate low coherence areas. At Mount Thorbjörn and its surroundings, the abrupt formation of a rift between 10 and 11 November 2023 causes decorrelation of the radar signal. (B) Wrapped interferogram of the same images in radar coordinates (Perpendicular baseline = 189 m). The fringes are closer together near the dyke-induced rift. Close-up views of the interferogram (C) in the north of, (D) on, and (E) in the southwest of the mountain. Black lines ('1') indicate the inferred active surface fractures previously mapped by Ducrocq et al. (2024) for the period December 2019 to March 2021. White lines ('2') correspond to the remaining identified active fractures in this study.

detailed representation of the topography and landscape at the time of data acquisition, which are the key elements for our study (Fig. 3). The high-resolution DEMs allow for the identification of the key morphological features that make Mount Thorbjörn a very distinctive landform.

Mount Thorbjörn has a height of about 200 m from its base. In plan view it has a roughly elliptical shape, elongated towards the NNE, with dimensions of 1.4 km in length and 1 km in width. The total volume of the mountain, calculated from drone DEM data, is 0.127 km^3 and presents varying slopes from base to summit. The lower part has steep slopes, ranging from 10° to 40°, with the steepest areas in the west associated with an inwardly curved ridge, previously described as a landslide scarp (Shevchenko et al., 2021).

At approximately 110 m above the base (bold contour line in the DEMs, Fig. 3), a break in the slope marks the transition to a plateau covering an area of around 0.5 km^2. Within the plateau, a 70 m high off-centre cone rises where the highest elevations occur. The NNE-SSW axial part of the mountain has subsided relative to the flanking regions along two subparallel normal faults, forming a prominent graben structure with significant displacements reaching 13 m (Shevchenko et al., 2021). Other less prominent fault scarps are also present. These are difficult to trace along their entire length because they are partially covered by a layer of regolith. Three main areas are defined on the basis of their azimuths: 5–15°, 20–30° (the most common) and 50–60°. Apart from these features, the plateau is mainly flat, with only subtle variations in elevation across its surface.

5.2.2. *New surface fractures mapped with the MTC*

MTC applied to subsequent high-resolution orthophotos of Mount Thorbjörn, supported by in-situ monitoring of fresh fractures, allowed us to identify a large number of new surface fractures that had developed during the analysis period (Fig. 4A). Most were first detected in the 18 November 2023 orthophoto, suggesting that the 10–11 November 2023 deformation episode was the most relevant in terms of its geomorphic impact on the mountain.

We identified 1829 new traceable fractures from July 2022 to August 2024, with a cumulative length of 9.1 km, further subdivided into 9112 segments of 1 m for statistical analyses. The uninterrupted fracture lengths ranged from 10 cm to 50 m, with an average length of 5 m, indicating that shorter uninterrupted segments predominated. 88 % of the total fracture length was detected in the November 2023 dataset, 12 % in April 2024 and less than 1 % in August 2024.

In the field, surface fractures were usually recognised as shear-related, with evidence of oblique movement including normal dip-slip and right-lateral strike-slip displacements. Tensile displacements were also evident in some localised sections. We identified normal dip-slip movement from fresh fault scarps along the fractures (Fig. 4C, D, E,

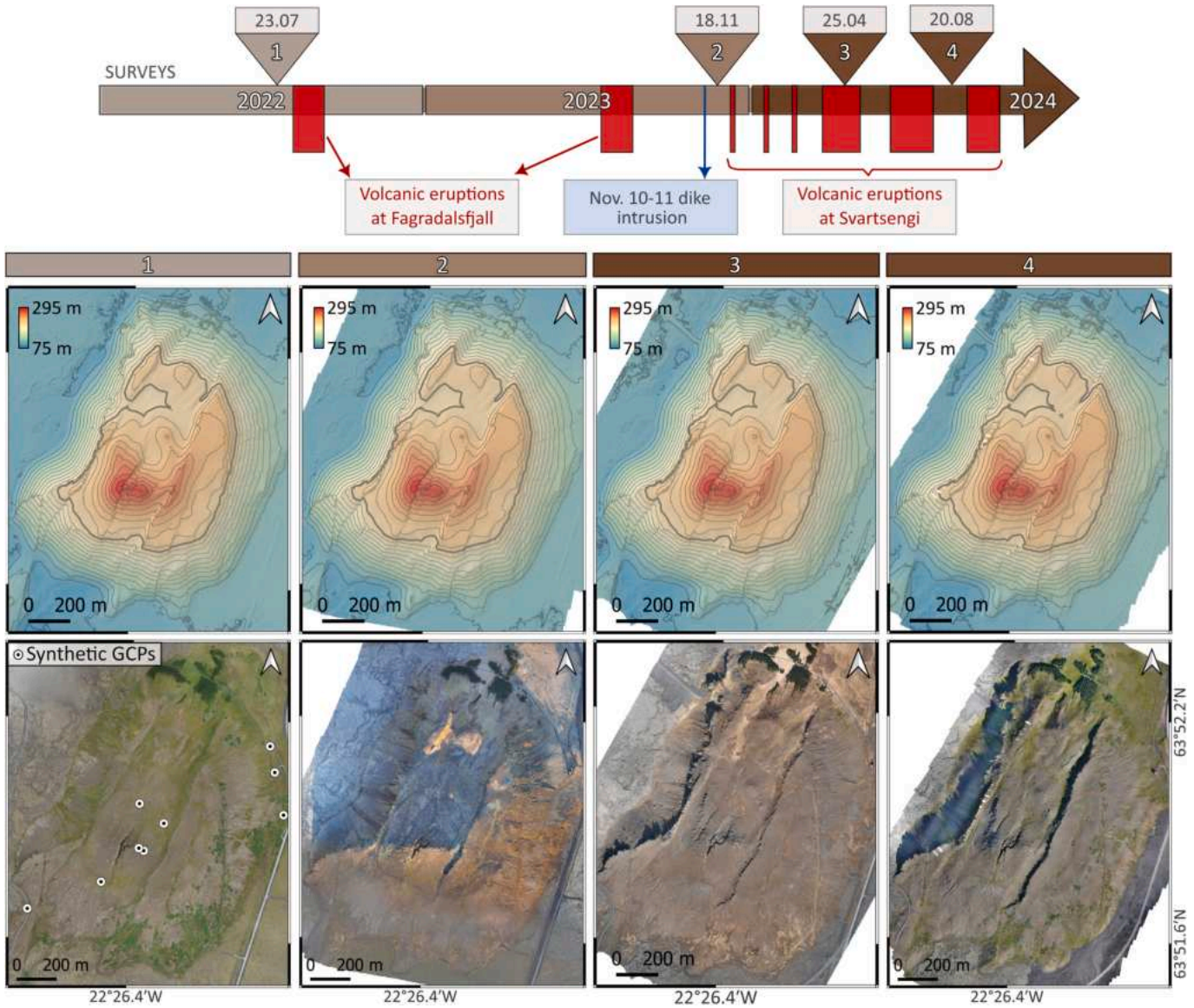

Fig. 3. Top: Timeline specifying data acquisition dates and relevant contemporary events. Bottom: DEMs and orthophotos derived from drone optical imagery acquired over Mount Thorbjörn during the successive surveys (here numbered 1,2,3,4). Contour lines are shown every 10 m, bold contour lines indicate the 210 m elevation, marking the approximate location of a slope break that defines the plateau. The synthetic GCP positions that were used to align the orthophotos, with reference to the 2022 dataset, are indicated by circle symbols in the bottom-left map.

H), with variable throws ranging from <10 cm to ~80 cm. We identified right-lateral strike-slip components through kinematic indicators such as left-stepping en-échelon arrangements of segments along the main fault plane (synthetic Riedel shears, Fig. 4D) and pull-apart structures along faults with undulating azimuth (Fig. 4E). We found tensile fractures where aperture was evident along the fracture plane (Fig. 4F), which appear to result mainly from fault-linking processes. Tensile displacements measured in the field range from 15 to 20 cm.

Fractures are typically spatially related to sinkholes (Fig. 4G), of variable dimensions, with lengths reaching up to 5 m, and often elongated following the azimuth of associated fractures, thereby suggesting the continuation of the fracture trace beneath the surface. During the analysis period, we identified 222 new sinkholes forming on Mount Thorbjörn (Fig. 4B, G) by comparing the orthophotos. Of these, 59 % became visible in November 2023, 39 % in April 2024, and 2 % in August 2024. Like the fractures, most sinkholes first observed in November 2023 continued to enlarge throughout the analysis period (Fig. S.3).

5.2.3. *Fracture kinematics using SaCDT*

To analyse the morphological change on Mount Thorbjörn after the dyke-induced deformation in November 2023, we used a combination of DEM of Difference (DoD) and Digital Image Correlation (DIC) methods.

We created a DoD map for 23 July 2022–18 November 2023, corrected it with data from the GNSS station THOB, and generated elevation difference profiles oriented transversely to pre-existing structures (Fig. 5). The DoD map (Fig. 5A) shows apparent vertical surface displacements, indicating subsidence in the mountain, that is more pronounced towards the southeast. Abrupt changes in colour between adjacent areas on the map may be associated with fault activity leading to sudden changes in the surface elevation, although in some cases they may be artifacts related to the mountain's horizontal drift. Such artifacts are particularly evident on the eastern and western slopes of the mountain, where horizontal movement projects in the DoD, leading to incoherent values such as apparent uplift on the western slope (Fig. 5A). This occurs because these effects are most pronounced in steep terrain, significantly affecting the signal, and are negligible in areas with gentle

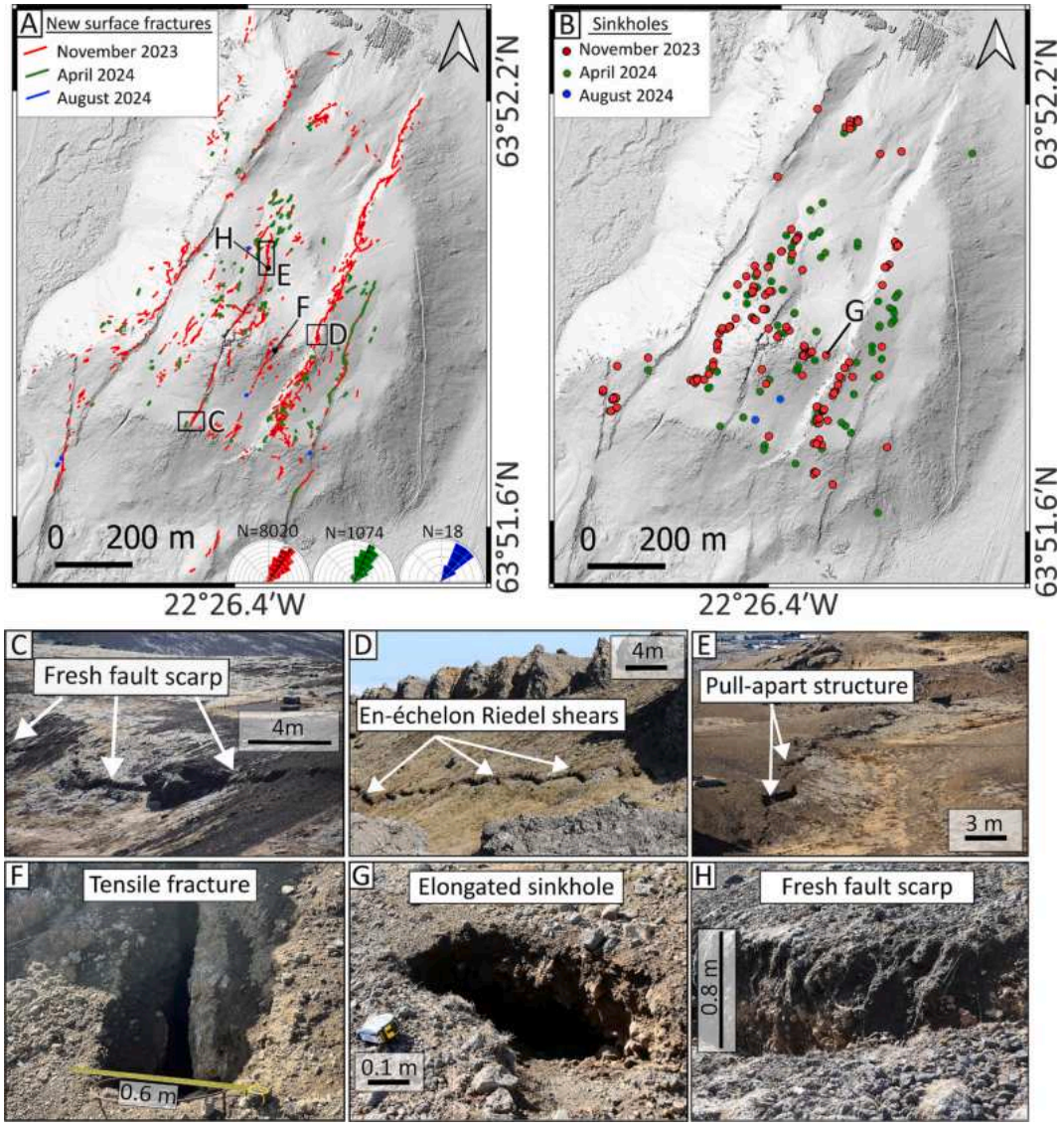

Fig. 4. DEM of Mount Thorbjörn with the mapped surface fractures (A) and sinkholes (B) in different colors according to the time when they became visible. (C) (D) and (E) show photos of the fault traces in the field taken in April 2024, where kinematic indicators can be seen. (F) (G) and (H) are close-ups of a tensile fracture, a sinkhole and a fresh fault scarp.

slopes.

To identify and correct for this, we calculated a Corrected Vertical Displacement (CVD) value by removing the effect of horizontal drift for each slope value along the transects (blue shaded profiles in Fig. 5B). This correction allowed us to verify and better estimate vertical displacements along the profiles. The resulting CVD profiles exhibit a stepped pattern, indicative of dip-slip shear along fault planes, which generally align with the previously identified abrupt colour changes on the DoD map.

To estimate relative offsets, we calculated average CVD values between fault planes (red horizontal lines, Fig. 5B), which range from ~10 cm to ~90 cm. On the western side of Mount Thorbjörn, the blocks east of the faults tend to move downward relative to the blocks on the west, whereas on the eastern side, the behaviour is reversed.

From north to south, the profiles show variations in relative offsets along the faults. Considering the average CVD of the westernmost and easternmost blocks of each profile, the cumulative displacements from north to south are +9 cm (A-A'), −33 cm (B-B′), −77 cm (C-C′) and −130 cm (D-D′). These values indicate a progressive increase in the eastward tilting of the mountain towards the south.

We further overlaid elevation profiles on each transect to compare pre-existing fault scarp positions with the recognised vertical offsets, which are generally aligned. We also illustrated fault activity at depth, though dip and down-depth directions remain unknown and are approximated based on fault traces and topography.

Using the DoD map and the CVD profiles, we assessed the relative vertical displacement of blocks associated with pre-existing fault scarps identified from orthophotos and DEMs (Fig. 5A). This analysis revealed reactivation along many pre-existing fractures. Compared to a DEM, most planes align with pre-existing fault scarps, suggesting fault reactivation. However, vertical displacements were not always recognised continuously along the entire length of the pre-existing scarps. In these cases, fault reactivation continuity was inferred and represented with a black dashed line in Fig. 5A. Conversely, in other areas, vertical offsets were observed in the DoD map, but no pre-existing fault scarp was visible, possibly due to the low relief of the scarp and sedimentary cover. In these cases, the DoD analysis revealed previously hidden pre-existing fault structures, highlighting some of the mountain's pre-existing structures. Such features can however be considered reactivations only when visible in both bedrock and sediments; if confined to sediments,

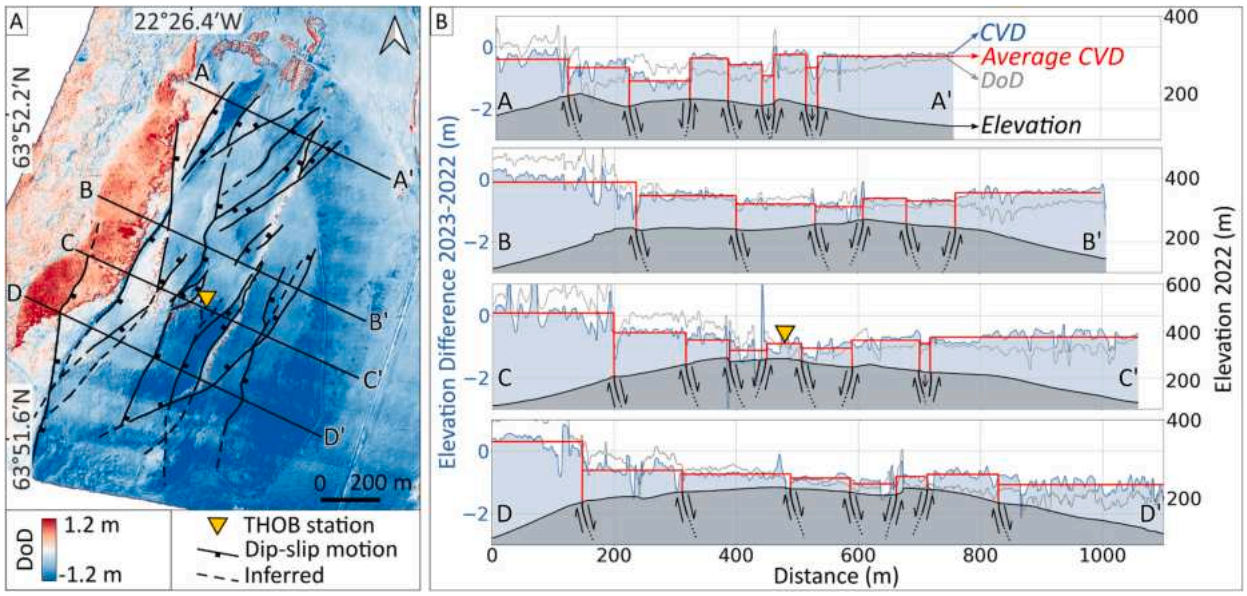

Fig. 5. (A) DEM of Difference (DoD) map for 23 July 2022–18 November 2023, corrected using the reference GNSS station THOB, indicated with a yellow triangle. (B) Profiles of the Elevation Difference: Grey lines represent DoD values from (A), used to calculate the Corrected Vertical Displacement (CVD, blue shaded). Vertical offsets define fault planes (black lines). Note that the dip and downdepth extension are shown schematically only. (For interpretation of the references to colour in this figure legend, the reader is referred to the web version of this article.)

their origin remains uncertain.

To investigate horizontal displacements along the identified active dip-slip fault planes, we calculated horizontal pixel offsets applying DIC to the two orthophotos from 23 July 2022 and 25 April 2024. We selected subsets at representative fault locations and first defined a local reference for each subset on one side of the fault (white cross in Fig. 6 B—F). Fig. 6A shows a hill-shaded DEM of Mount Thorbjörn with the location of the analysed subsets, where we identified horizontal displacements associated with strike-slip activity. Fig. 6 (B—F) show Y-displacement maps (north-south direction) obtained by DIC where strike-slip shear is evident. The colour scale in each case illustrates the relative movement on either side of the faults, with the western blocks moving northwards with respect to the eastern blocks. Given the azimuths of the fault segments (NNE and NE), these northward displacements result in right-lateral strike-slip components. The boundary between blocks is exactly where dip-slip faults have been identified using DoD. These fault segments are NNE- and NE-striking and usually form interconnected conjugate segments. The method allows quantification of the relative northward displacement, which is on the order of ~20–30 cm in most cases. The oblique kinematics observed along the fault planes, identified combining change detection techniques (DoD, DIC), are consistent with field observations of recent faults on Mount Thorbjörn (section 5.2.2).

5.3. Linking recent fracture activity to pre-existing mountain morphology

5.3.1. Reactivation

We analysed the spatial relationship between new surface fractures and pre-existing fractures to test reactivation processes (Fig. 7A). Surface fracture density plots were generated for 25 subsections of the DEM, and their distribution was examined in relation to the older structures (Fig. 7B). The resulting map evidences how fracture density peaks are generally located at or near the pre-existing fractures, with some sectors exhibiting a more pronounced asymmetry in this regard, particularly in areas where fractures are abundant (Fig. 7B). To the west, where the slopes are very steep within the landslide scarp, some peaks do not appear to correlate with any pre-existing fracture.

5.3.2. Fracture density

The density of recently visible fractures was analysed in relation to

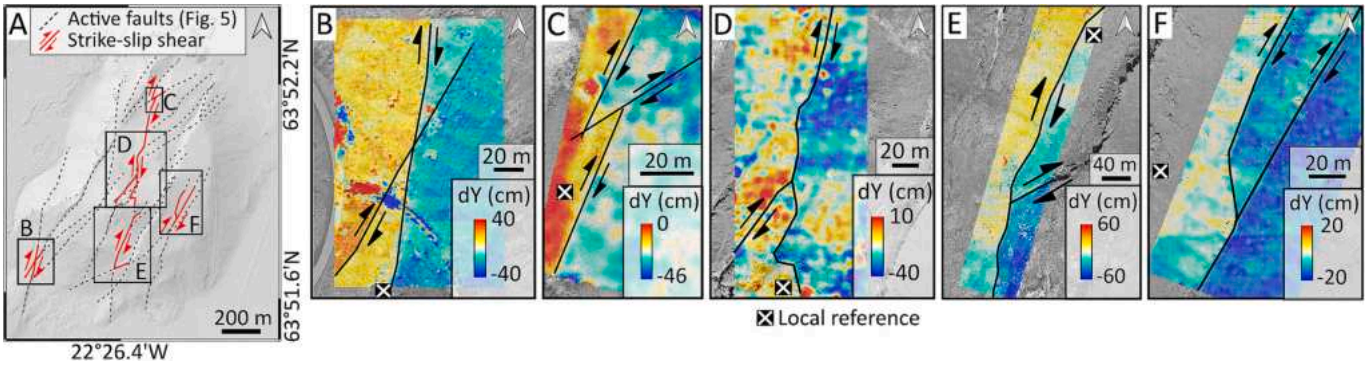

Fig. 6. (A) Hillshade DEM of Mount Thorbjörn showing the previously mapped normal faults as dashed black lines and identified right-lateral strike-slip displacement using DIC, shown as red lines. (B—F) show the DIC displacement maps of each subset in the Y direction. The values are relative to a reference point for each subset, indicated by a white cross. Blocks shown in warmer colors moved northward relative to adjacent blocks in colder colors. (For interpretation of the references to colour in this figure legend, the reader is referred to the web version of this article.)

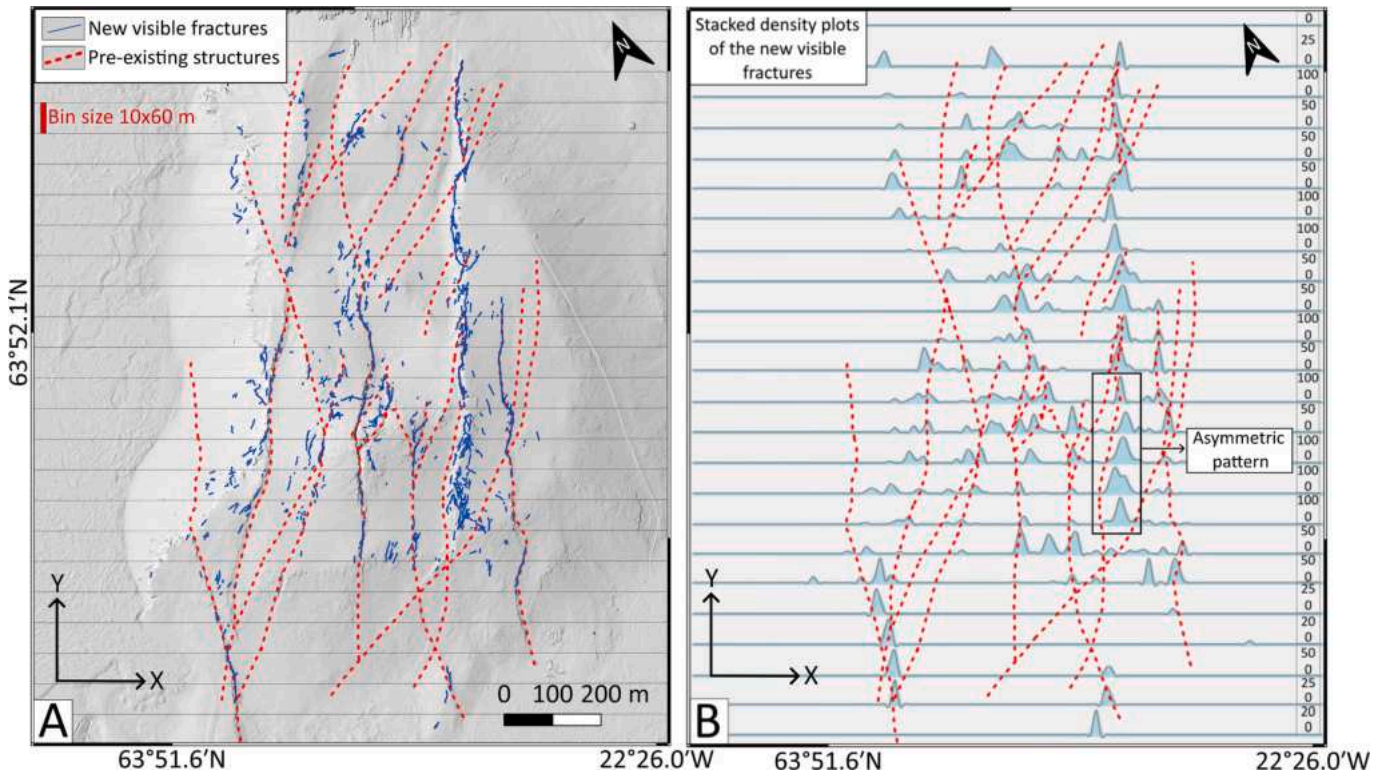

Fig. 7. (A) Hillshade DEM of Mount Thorbjörn. Blue lines represent the traces of fractures visible since November 2023, while red dashed lines indicate the interpreted pre-existing faults of Mount Thorbjörn. The map has been rotated 23 degrees counter-clockwise to align the structures in the Y direction. We have divided the map into 25 subsections of the DEM along the Y axis, each 60 m high. The bin size used for the analysis in B is shown in the upper left corner. (B) Vertically stacked fracture density plots calculated for each subsection of the DEM shown in (A), overlaid on the interpreted pre-existing faults. (For interpretation of the references to colour in this figure legend, the reader is referred to the web version of this article.)

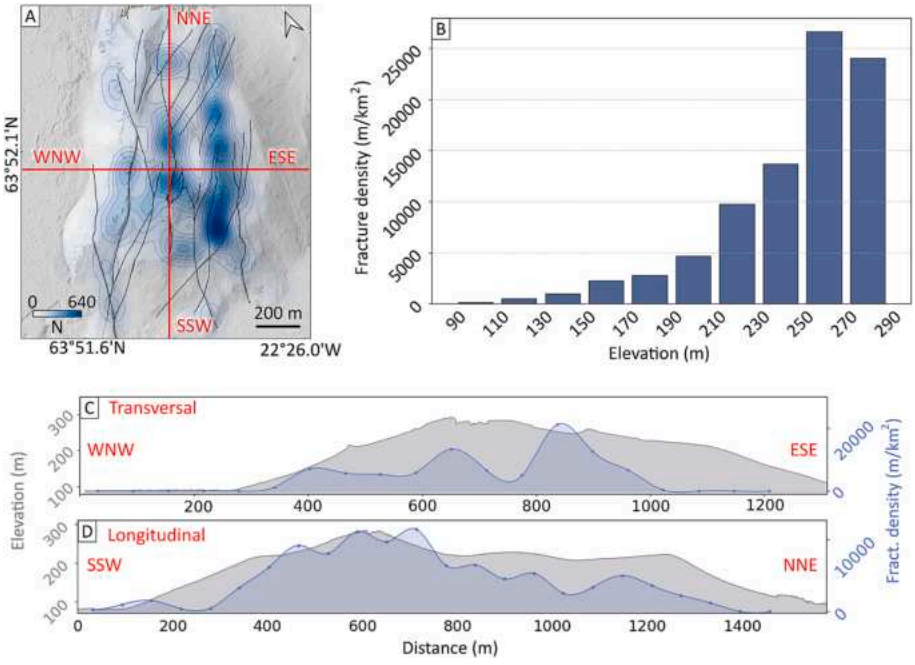

Fig. 8. (A) Hillshade DEM of Mount Thorbjörn, rotated 23° counterclockwise, overlaid with a 100 m radius Kernel Density Estimation map showing the density of 1 m fracture segments. Blue tones indicate higher concentrations of segments, which accumulate in the highest elevation sectors. Black lines correspond to the pre-existing fractures. (B) Histogram of fracture density versus elevation. For each elevation range represented by a bar, the cumulative fracture length was calculated and normalized by its area. (C) and (D) Elevation profiles (grey) and corresponding fracture density profiles (blue) along the WNW–ESE and SSW–NNE transects shown in (A), respectively. Fracture density was calculated every 60 m along each profile using 60 m-wide DEM subsections and interpolated with a cubic spline to produce smooth curves. Each value represents the cumulative fracture length within a subsection, normalized by its area. (For interpretation of the references to colour in this figure legend, the reader is referred to the web version of this article.)

topography to assess potential correlations that might reveal topographic controls. We created a density map showing the distribution of 1 m fracture segments across the mountain, which we overlaid on a DEM (Fig. 8A). The map was generated using the Kernel Density Estimation function in QGIS, with a 100 m radius and a Quartic kernel. Each fracture segment contributes then to the density within the radius, creating a visual representation of the distribution of fractures useful for identifying patterns. Fractures are predominantly located within the plateau and nucleate close to pre-existing features of the mountain, in particular the two prominent fault scarps to the west and east of the mountain (Fig. 8A). The highest density peak in the map is in the southern part of the eastern fault scarp, one of the highest points on the mountain.

We then calculated the fracture density values considering elevation ranges. For this, we divided the data into elevation intervals, calculated the cumulative fracture length within each interval, and normalized it by the area of each elevation range to obtain the metres of fractures per km^2. The histogram in Fig. 8B shows a clear correlation between elevation and fracture density.

To gain a more detailed insight into the interaction between topography and fracture density, we created two topographic and fracture density profiles oriented WNW–ESE and SSW–NNE, respectively (red lines in Fig. 8A). These correspond to transversal and longitudinal sections relative to the average structure orientation at Mount Thorbjörn. For both profiles, fracture density was calculated every 60 m using 60 m-wide subsections of the DEM, perpendicular to each profile. These values were then interpolated using a cubic spline method to generate a continuous, smooth curve that avoids abrupt changes, allowing for a clearer comparison between elevation and fracture density variations.

The transversal profile (WNW–ESE, Fig. 8C) presents three peaks in fracture density. A small peak occurs on the steep northwestern slope of the mountain, likely associated with slope instability processes favouring local fracturing. The two remaining peaks are located within the plateau, around the highest elevations of the hill. The highest density values are found on the southeastern side of the mountain, corresponding to the area that experienced the greatest subsidence during the November 2023 deformation episode (Fig. 5B). This spatial correlation suggests a causal relationship, in which greater subsidence is associated with more intense fracturing.

The longitudinal profile (SSW–NNE, Fig. 8D) follows a transect that crosses the main topographic features of Mount Thorbjörn (i.e., the steep slopes from the base of the mountain to the plateau, the plateau and the off-centre cone within the plateau), which makes it useful to test topographic controls on fracturing. This profile shows a correlation between elevation and fracture density (Fig. 8D), as peaks in fracture density align with local topographic highs, particularly clear at the off-centre cone.

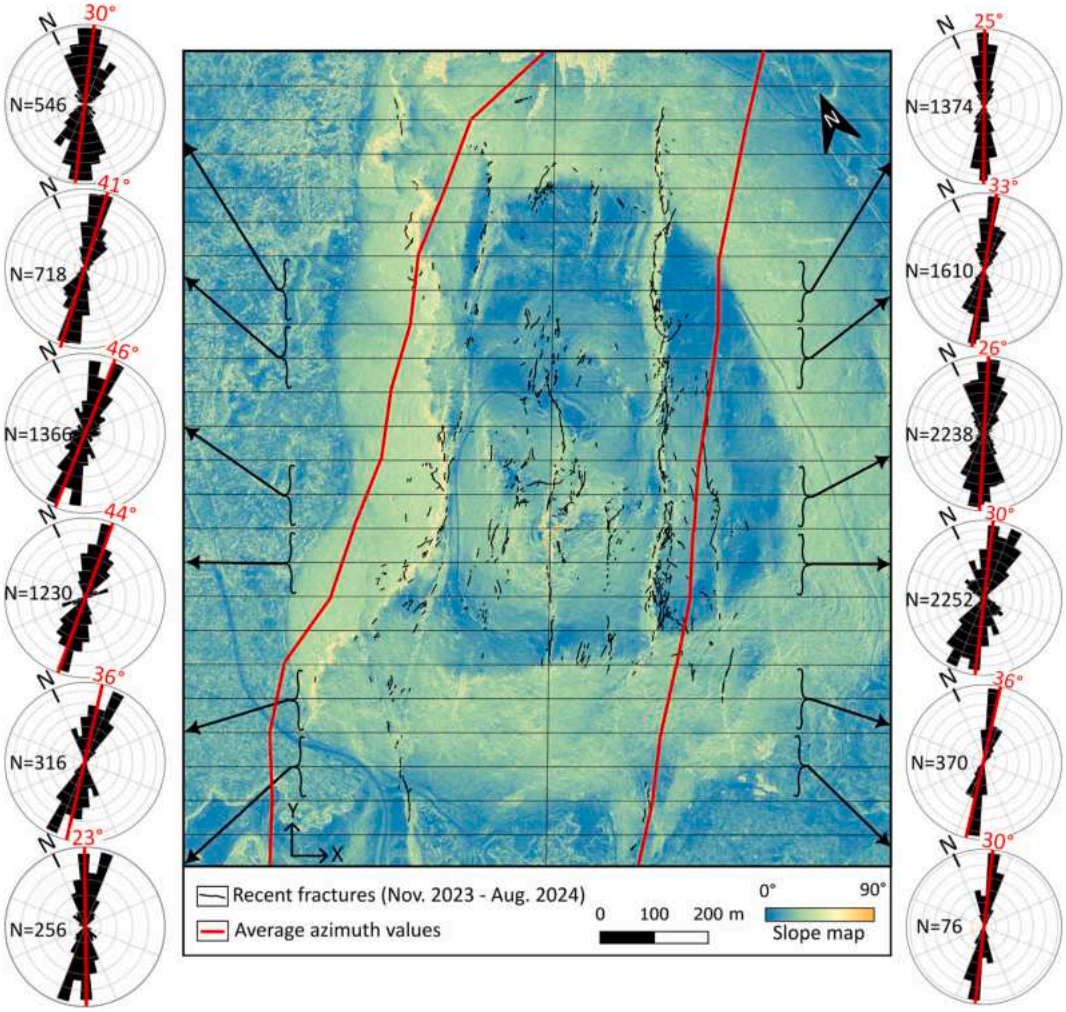

Fig. 9. Slope map of Mount Thorbjörn, subdivided into a western and an eastern sector. The map was rotated by 23° to align structures with the Y direction. Fractures are mapped in black, and rose diagrams represent the fracture azimuth distribution for each pair of subsections along the Y direction. Red segments and numbers on the rose diagrams indicate the average azimuth, while black numbers represent fracture counts. Red curves overlaid on the slope map result from all calculated average values along the Y direction. (For interpretation of the references to colour in this figure legend, the reader is referred to the web version of this article.)

5.3.3. Fracture azimuth

To further investigate the behaviour of recent fracture azimuth across the area of interest and test possible relationships with pre-existing mountain morphology, we analysed the fracture azimuth distributions. We divided the previously rotated map from Fig. 7A into a west and an east side and created a rose diagram for every two subsections of the DEM. We also calculated the average for each rose diagram, shown as a segment, which we connected vertically to create a curve representing the average values along the Y axis for each side of the map. The result is shown in Fig. 9, which presents a slope map of the area with some selected representative rose diagrams from the analysis and the average azimuth value as red lines.

On the eastern side, rose diagrams show low variability in the south and north. However, a wider range of values indicates increased variability in the central region, particularly within the off-centre cone in the plateau. In terms of average azimuth values, a reasonably linear trend is observed in the eastern sector along the length of Mount Thorbjörn. This trend implies that the most common values remain stable, falling between 26° and 36°. Looking at the three main patterns of pre-existing fracture orientations on the mountain (5–15°, 20–30° and 50–60° azimuth), we find that these average values closely match the average azimuths of the pre-existing fractures.

In contrast, the western sector shows greater variability along the Y axis. Along the western flank of the mountain, several fractures result from slope instability processes on the steep, crescent-shaped, concave landslide scarp. They are typically oriented perpendicular to the maximum dip direction of the surface, which varies considerably along the length of the fracture surface. In the southern part, outside the landslide scarp, average azimuths are relatively stable, ranging between 23° and 25°. In the central part, within the landslide scarp, average fracture azimuths decrease towards the north from 58° to 30°. To the north, where the fracture surface is less prominent, average fracture azimuths increase again, ranging from 46° to72°.

6. Discussion

Regions with complex topography exhibit diverse deformation patterns during seismic and volcanic events, yet the relationship between topography and fracturing remains understudied. This work sheds light on the structural geology and deformation during the 2023–2024 volcanic unrest within the Svartsengi Volcanic System on the Reykjanes Peninsula, Iceland, with a focus on the dyke-induced graben episode of 10 November 2023. Using four drone photogrammetry datasets from 2022 to 2024, we analysed Mount Thorbjörn, a ~200 m high glacio-volcanic edifice on the western graben shoulder. Our high-resolution orthophotos and elevation models reveal transtensional reactivation of pre-existing grabens, with normal dip-slip offsets up to ~80 cm and dextral strike-slip of ~20–30 cm, particularly in the southeastern sector, with important implications for the general volcano-tectonic coupling discussed further below. Orthophoto comparisons allowed us to map new fractures with a cumulative length of over 9 km and 222 sinkholes, with most fractures and sinkholes forming between 23 July 2022 and 18 November 2023, likely due to the November 2023 graben event. Statistical analyses highlight strong topographic controls on fracture distribution and geometry, supporting a conceptual model of fracture development in complex terrain during volcanic unrest.

6.1. Limitations of the drone dataset

Our data and analysis methods have limitations, such as the temporal resolution of the datasets (Fig. 3). Our four datasets cover a period of 2 years and 1 month, from July 2022 (the first acquisition) to August 2024 (the last acquisition), with two additional datasets in between (November 2023 and April 2024). Therefore, the temporal resolution includes intervals of 1 year and 4 months (July 2022–November 2023), 5 months (November 2023–April 2024) and 4 months (April 2024–August 2024) respectively. Between the first and last acquisition, periods of magma accumulation at Svartsengi caused surface inflation, followed by seven dyke intrusions causing surface subsidence, five of which resulted in eruptions (De Pascale et al., 2024; Pedersen and Grosse, 2014; Sigmundsson et al., 2024; Troll et al., 2024). Due to the temporal resolution of our data, we assume that the main fracture activity resulted from a single significant event and attribute it to the November 2023 graben event.

Another limitation is related to the DoD map generation. Although the DEMs used in this study were acquired using a GNSS base station connected to the drone via an RTK antenna, which provides high accuracy in the geolocation of the images collected during the drone flights (Lewicka et al., 2022), the most reliable results are obtained when integrated with GCPs. We used the THOB GNSS station as an external control point. Additional points would have been beneficial to correct for distortions in the DEMs, but it was not possible to establish benchmarks at the beginning of the crisis. In addition, the correction applied to the elevation difference profiles for horizontal displacements assumes a single representative horizontal displacement vector for the entire study area, which is also a simplification.

The drone image data were analysed using DIC, which is widely used to measure surface deformation with high accuracy and has previously been applied to deforming volcanoes (James et al., 2020; Walter, 2011; Zorn et al., 2020). The pixel size (here ~10 cm) defines the detectable displacement; after applying a sub-pixel registration algorithm, the displacement measurement can achieve an accuracy smaller than a single pixel (Pan et al., 2009). However, the accuracy and applicability are limited by other factors (Walter, 2011), including lighting effects, surface changes (e.g., vegetation growth, moisture variations), and overall image quality. These factors alter the pixel intensity and, consequently, the quality of the correlation. Quantifying the uncertainty introduced by these effects is extremely challenging and beyond the scope of this paper, and therefore remains speculative. Yet, acknowledging these limitations is essential for optimising DIC applications. In this study, we have selected subsets minimally affected by such factors, ensuring that the overall deformation pattern remained coherent despite minor artifacts.

6.2. Complimentary traditional geodetic techniques at Mount Thorbjörn

InSAR was used to identify previous inflation cycles that affected Mount Thorbjörn in 2020 (Flóvenz et al., 2022) and to identify fault reactivations prior to the 2023 unrest (Ducrocq et al., 2024). During the November rift event, InSAR captured large-scale motion and fault reactivation at a distance from Mount Thorbjörn (De Pascale et al., 2024; Sigmundsson et al., 2024). However, in the steep terrain of Mount Thorbjörn, InSAR is inconclusive due to decorrelation and coherence loss (Fig. 2), with large vertical displacement values that do not align with the range offsets and seem to indicate local deformation associated with graben faulting (see Supplementary Information in Sigmundsson et al., 2024). Therefore, not much information can be extracted from InSAR at this location, even using short wavelength radar imagery. Coherence increases north and south of the mountain, probably indicating that the line-of-sight shift was more pronounced in the mountain than in the surrounding area.

GNSS has been used for decades to monitor the geodynamics of the Reykjanes Peninsula, including our study area (Sigmundsson et al., 2020). This amplification of the displacement at the topographic high of Mount Thorbjörn is further confirmed by GNSS data provided by the Icelandic Meteorological Office's public database (https://aflogun.vedur.is/), also reported by Sigmundsson et al. (2024). The locations of the relevant stations are shown in detail in the supplementary Fig. S.1. At Svartsengi, GNSS data recorded during the November 2023 graben episode show a westward decrease in vertical displacement from Grindavík (De Pascale et al., 2024; Sigmundsson et al., 2024). Station GRIC recorded −110 cm of vertical displacement between 10 and 11

November, with decreasing displacement values at stations THOB (−86.1 cm) and HS02 (−33 cm), consistent with typical graben deformation profiles. Perpendicular to the GRIC-THOB-HS02 alignment, the SENG-HS02-SKSH alignment exhibits stable vertical displacements ranging from −33 to −41, which are 2 to 3 times lower than those at GRIC, despite differences in station distances. These observations suggest that local factors at THOB may have amplified the displacement beyond what elastic models predict based on the spatial relationship to the graben (Sigmundsson et al., 2024).

6.3. Drone insights on fracture reactivation and topographic controls

Dominant N*E*-striking normal faults and fissure swarms as well as N-striking right-lateral strike-slip faults have been identified on the Reykjanes Peninsula in early geological surveys (Jónsson, 1978). Satellite imagery, aerial photography and DEMs, combined with other data sources (e.g., seismic, GPS), have led to detailed structural maps and enhanced understanding of the region's fracture dynamics (Clifton and Kattenhorn, 2006; Ducrocq et al., 2024; Einarsson et al., 2023). In this study, we used cm-resolution drone-derived orthophotos and DEMs, combined with field observations, to analyse fracture geometry, distribution and kinematics during the recent volcano-tectonic event in Svartsengi, providing insights into fracture dynamics at topographic highs.

6.3.1. Structure reactivation and kinematics

Well before the onset of the Reykjanes Peninsula's rifting event in 2020, Gudmundsson (1987) had already suggested that fractures in postglacial lava flows were surface expressions of old Pleistocene structures hidden beneath younger lavas. Subsequent studies have provided further evidence of fracture reactivation across the peninsula (Clifton and Einarsson, 2005; Clifton and Kattenhorn, 2006). Since 2020, remote sensing data supported by field observations have documented continuous displacement along pre-existing fractures (Bufféral et al., 2023; Ducrocq et al., 2024; Hjartardóttir et al., 2023). Similar fracture reactivation processes directly related to dyke intrusions have been observed at other sites in Iceland, including western Iceland (Khodayar and Einarsson, 2002), and more recently during the 2014 Bárðarbunga volcano-tectonic episode (Ruch et al., 2016).

The use of DoD and DIC in this study allowed us to detect vertical and horizontal displacements along fault planes at Mount Thorbjörn, many of which followed pre-existing fault scarps at the surface. In contrast, others represented their buried continuations, lacking clear surface scarps. On one hand, this provides key insights into the role played by fracture reactivation in this context, as deformation during the 2023–2024 volcano-tectonic event was accommodated by reactivation of pre-existing fractures, without evidence of new fractures being formed at this location. On the other hand, the results highlight the complex and partially hidden nature of the fracture network at Mount Thorbjörn, which may represent a common pattern across the Reykjanes Peninsula. The combination of change detection techniques thus provides a way to identify deformation despite sediment cover, allowing a more thorough understanding of the structures in the region.

The fracture reactivation that we recorded shows both normal and oblique displacements along N, NNE, and NE-striking fractures. This kinematics has previously been identified as the most common during magmatic periods on the Reykjanes Peninsula (Clifton and Kattenhorn, 2006). Oblique motion along fractures, including right-lateral and normal displacements, occurred on conjugate N- and NNE-striking fractures. Together, they form curved and anastomosing fracture zones, usually defining shear lenses of varying dimensions. This pattern is commonly observed in transtensional settings (e.g., Wesnousky, 2005) and has previously been described in other rift sectors on the Reykjanes Peninsula, such as in the Vogar Graben (Clifton and Kattenhorn, 2006; Gudmundsson, 1987). There, the pattern consists of NE-striking normal faults and E-striking open fractures, which have previously been suggested to be of different ages but to have interacted during transtensional periods (Clifton and Kattenhorn, 2006). Analogue experiments simulate similar patterns under transtensional conditions, and the final fracture morphology varies with rift obliquity (Clifton et al., 2000).

Ruch et al. (2016) investigated transtensional fracture reactivation during the 2014–2015 rifting event at Bárðarbunga (Iceland), an oblique rift setting. By calculating the extension and shear deficits accumulated during inter-rifting periods, they demonstrated that the sudden surface displacements during the co-rifting event aligned with the long-term deficit buildup. Similarly, we present evidence of oblique fracture displacement during the November 2023 rifting event at Svartsengi, possibly releasing a stress build-up from the previous centuries. In total we find a ~1 m dextral strike-slip component localised along five main fractures on Mount Thorbjörn.

This demonstrates how dyke-induced rifting in oblique rift settings can be related to both the dyke-induced extensional forces and the accumulated tectonic transtension, highlighting the dynamic interaction between magmatism and tectonics during such events.

6.3.2. Fracture distribution and geometry

The state of stress in a region varies considerably between different topographic settings (Miller and Dunne, 1996; Ziegler et al., 2016). Such stress variations can manifest as fractures with spatial distributions and orientations closely related to the shapes of the landforms (Miller and Dunne, 1996). At Mount Thorbjörn, recent fractures show an increasing trend in density with elevation (Fig. 8B), illustrating this process. Fractures are rare on the base slopes and become denser within the plateau, usually nucleating around the cone, fault-related cliffs on the plateau's west and east sides, and the curved landslide scarp along the western slope (Fig. 8A). This pattern suggests that recent fracture activity on Mount Thorbjörn has been more pronounced at higher elevations, particularly on peaks and unstable slopes, suggesting that topographic highs are vulnerable regions during volcano-tectonic events.

Apart from topographically-induced stresses, the topographic effect on fracture density may be related to other factors such as lithology (Havenith et al., 2003), groundwater (Clifton et al., 2003), and its influence on seismic wave amplification (García-Pérez et al., 2021; Massa et al., 2010). Deformation models and inversions should therefore include topography, as neglecting it can lead to incorrect interpretations (Hickey et al., 2024 and references therein).

Geometric variations in dyke-induced grabens due to topographic effects have been observed in volcanic regions, including Laki and Bárðarbunga in Iceland (Müller et al., 2017; Trippanera et al., 2015), Cumbre Vieja on La Palma (Walter et al., 2023), Harrat Lunayyir in Saudi Arabia (Trippanera et al., 2019), and Mount Etna in Italy (Tibaldi et al., 2022). In all cases, graben faults observed on flat surfaces diverge when encountering topographic highs, resulting in the widening of the graben.

Sandbox analogue experiments that consider conical and ridge-like topographies have supported natural observations (Trippanera et al., 2015; Walter et al., 2023) and reproduced the lens-shaped fractures observed in such environments. Inspired by these findings, we conducted simplified sandbox analogue experiments to investigate how Mount Thorbjörn's topography may have influenced fracture geometry during the development of its pre-existing fracture network. We designed these experiments to simulate tensile faulting beneath different topographic settings, including a flat surface, a flat-topped mountain, and a flat-topped mountain with an off-centre cone on top, closely resembling Mount Thorbjörn's geometry. The experiments show that fractures, which develop subparallel to each other under flat conditions, diverge when encountering topographic highs, forming lens-shaped structures. These geometries resemble those observed in nature, as observed in the drone data. Despite the simplifications, the experiments underscore the significant impact of slope and topographic features on fracture propagation, reinforcing the notion that topography played a

crucial role in shaping the mountain's pre-existing fracture pattern. The methodology and results of these experiments are included in the Supplementary Material.

6.4. Conceptual model

Our observations allow developing a conceptual model that highlights the following five elements. (1) On 10 November 2023, dyke-assisted subsidence within the Svartsengi Volcanic System affected a considerable area of the western Reykjanes Peninsula. InSAR and GNSS data revealed an unusually high vertical displacement at Mount Thorbjörn, suggesting enhanced deformation in this region (Fig. 10A).

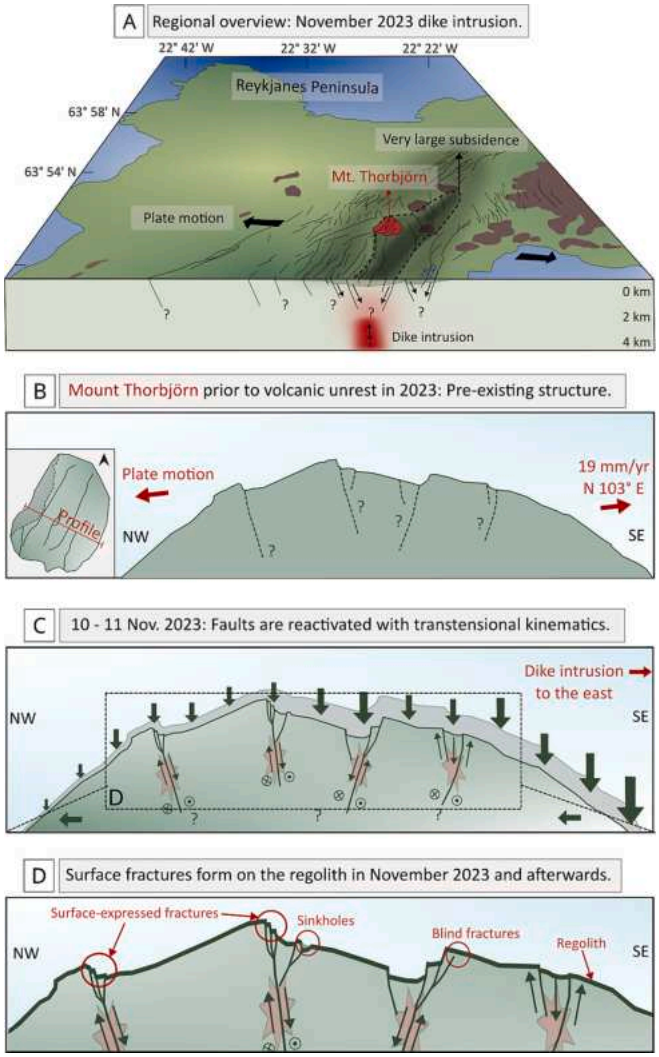

Fig. 10. Conceptual model of volcanic deformation consequences on Mount Thorbjörn since November 2023. (A) On 10 November 2023, a graben formed within Svartsengi reactivating fractures across the Reykjanes Peninsula. InSAR and GNSS data revealed high vertical displacement at Mount Thorbjörn, likely amplified by topographic effects. Active faults are shown in black, mapped using the TerraSAR-X interferogram from Fig. 2B. Fault dip and depth are illustrative. (B) Mount Thorbjörn, a highly fractured glaciovolcanic edifice, shows escarpments from retrogressive erosion of old fault scarps. Only selected faults are shown, with inferred dip and downdip extent. Plate motion from DeMets et al. (2010). (C) The November dyke intrusion caused significant subsidence and tilted Mount Thorbjörn toward the southeast. Pre-existing fractures in the mountain were reactivated with oblique kinematics. (D) Reactivation led to many surface-expressed and blind fractures and sinkholes that nucleate close to the pre-existing structures. Fracture patterns reflect the long-term morphology of the mountain and the transtensional tectonics.

(2) Drone data acquired before and after the dyke intrusion and graben formation confirmed high vertical displacements throughout the mountain, most pronounced in the southeast part, suggesting a tilting of the mountain (Fig. 10B, C). (3) Subsidence was largely accommodated by transtensional reactivation of pre-existing fractures, possibly triggered by stress changes due to dyke-induced deformation or strong ground shaking. Fracture activity included normal dip and right-lateral strike-slip displacements (Fig. 10C). (4) Deep fracture reactivation induced secondary surface fractures and sinkholes that cut through the regolith at the surface of Mount Thorbjörn (Fig. 10D). (5) The fracture pattern suggests that its development was controlled and favoured by a combination of factors, including the pre-existing fractures, the pre-existing topography, the amount of ground displacement, and the tectonic regime. While most of these surface features formed in November 2023, they continued to evolve progressively over time.

Given that the state of fracturing in a region plays a key role in relevant external geomorphic (e.g., erosion, slope instability, water infiltration) (Molnar et al., 2007) and internal geodynamic (e.g., magma movement to the surface, hydrothermal circulation) (Le Corvec et al., 2013) processes, a thorough understanding of the topographic controls on fracturing is key to assessing these processes. In volcanically active regions, fractures can serve as magma pathways to the surface and potentially control eruption sites, so we need to assess this complex interaction.

In Svartsengi, magmatic activity is extensively monitored (e.g., Barsotti et al., 2023). However, fracture activity has caused multiple disruptions across the entire region. Our results suggest that higher elevation zones containing pre-existing fractures are particularly vulnerable to being affected by these processes. However, the risk is not restricted to these sectors only, and the effects have been observed in the town of Grindavík (Fig. 1, S.1).

The presence of tensile fractures below the soil surface is significant in the region, as evidenced by the sinkholes identified on Mount Thorbjörn after the recent crisis, but also present in other sectors like Grindavík. Sinkholes form when the soil cover seeps into a fracture, resulting in structures that can be very large depending on the thickness of the sediment (Einarsson, 2010). As they are hidden underground, it is difficult to define the exact locations where sinkholes can occur, making them a major hazard. In addition, the formation and growth of sinkholes can continue for several years. At Mount Thorbjörn, sinkholes became visible in November 2023 and continue to develop, posing a high risk to anyone or any vehicle passing over them. While it is difficult to define areas where sinkholes may develop, detailed structural mapping such as the one we present here can help identify sectors where blind fractures with tensile components may exist. At Mount Thorbjörn, for example, tensile fractures have been identified as shear-related extensional steps, commonly fault linking zones. Identifying such zones may therefore provide clues to the hidden presence of tensile fractures, potentially leading to sinkhole formation in the future.

7. Conclusions

We have used multitemporal drone photogrammetric data to investigate the deformation and structural geology on Mount Thorbjörn following the Svartsengi 2023–2024 unrest phase, focusing on the dyke-induced deformation in November 2023. The main results of our analysis can be summarised as follows: (1) Fracture reactivation played a key role in accommodating the deformation. (2) Fractures moved dip-slip (~10–90 cm) and with additional dextral strike-slip (~20–30 cm) components that reveal an influence of the oblique rift forces. (3) Our data show subsidence and eastward tilting of the mountain, most pronounced in the south, where a 1.3 m difference in subsidence was evidenced between the west and the east. Subsidence at Mount Thorbjörn was enhanced relative to the surrounding low-lying areas, suggesting an amplification of the deformation in the highlands of Mount Thorbjörn. (4) A cumulative length of over 9 km of new surface fractures developed,

spatially related to the pre-existing structures. Over 200 sinkholes accompanied this trend and location. (5) Their spatial density increases with elevation and clusters around local topographic features on the mountain, confirming increased deformation at higher elevations. (6) The continuous evolution of these structures, particularly in relation to sinkhole formation, highlights the need for continuous monitoring to manage associated risks. Our work highlights the power of multi-temporal drone data to study fracture dynamics in active volcanic regions: while satellite-based techniques (e.g., InSAR and GNSS) are useful for regional-scale monitoring and denser temporal sampling, periodic drone surveys remain essential for capturing small-scale features such as the fractures and sinkholes identified in this study.

CRediT authorship contribution statement

Maria Hurley: Writing – original draft, Visualization, Validation, Supervision, Software, Project administration, Methodology, Investigation, Funding acquisition, Formal analysis, Data curation, Conceptualization. **Nicolas Oestreicher:** Writing – review & editing, Validation, Methodology, Investigation, Formal analysis, Conceptualization. **Alina V. Shevchenko:** Methodology, Investigation, Data curation. **Gregory P. De Pascale:** Writing – review & editing, Validation, Investigation. **Magnús T. Gudmundsson:** Writing – review & editing, Validation, Supervision, Resources, Investigation, Data curation. **Egill Á. Gudnason:** Validation, Resources, Data curation. **Gylfi P. Hersir:** Validation, Resources, Data curation. **Benjamin F. De Jarnatt:** Methodology, Data curation. **Alea Joachim:** Methodology, Data curation. **Joël Ruch:** Validation, Supervision, Conceptualization. **Fabio L. Bonali:** Writing – review & editing, Validation, Supervision, Conceptualization. **Thomas R. Walter:** Writing – review & editing, Validation, Supervision, Resources, Methodology, Investigation, Funding acquisition, Conceptualization.

Declaration of competing interest

The authors declare that they have no known competing financial interests or personal relationships that could have influenced the work reported in this paper.

Acknowledgements

We would like to thank Sophia Bäurich, Edgar Zorn, Ai Lun, Elisa Piispa and Isabella Feldmann for their assistance in the field. We also thank the Icelandic Centre for Research (Rannís) for issuing a Research Declaration, the Department of Civil Protection and Emergency Management (Almannavarnir) for facilitating access to the eruption site, and the local emergency team in Grindavík for their support during fieldwork. This work was supported by a Hazard Assessment and Risk Task Force project [HART-2023]. It was made possible with the support of a scholarship awarded to M.H. by the German Academic Exchange Service (DAAD). B.F.D.J. and T.R.W. are financially supported by ROTTnROCK, a research project funded by the European Research Council under the European Union's Horizon Europe Programme [ERC-2023-SyG 101118491].

Appendix

Table A1
Summary of the drones used for each survey, key features, flight details and processing results.

Survey	1	2	3	4
Date	**23 July 2022**	**18 November 2023**	**25 April 2024**	**20 August 2024**
Drone model and positioning system	DJI Phantom 4 RTK		DJI Matrice 30T RTK	WingtraOne PPK fixed-wing
Camera type	1″ CMOS and 20 MPixel		½″ CMOS and 12 MPixel	Full-frame and 61 Mpixel Sony Alpha 7 Mark IV
Altitude control mode	Constant height: ~ 120 m above summit		Constant height: ~ 90 m above summit	Follow-terrain: ~ 150 m above ground
Images Overlap			70 % lateral and 80 % frontal	
Images used for SfM and number of tie points	857 images 745,833 points	473 images 690,453 points	2550 images 1,362,554 points	806 images 1,007,994 points
DEM Pixel Resolution	16.7 cm/pix	20 cm/pix	13.7 cm/pix	6 cm/pix
Orthophoto Pixel Resolution	8.4 cm/pix	10 cm/pix	6.8 cm/pix	3 cm/pix

Appendix A. Supplementary data

All data used in this article can be found online in the Supplementary at https://doi.org/10.1016/j.jvolgeores.2025.108407.

Data availability

Data is accessible via the following link: https://doi.org/10.5880/GFZ.HDBG.2025.001

References

Acocella, V., 2021. Volcano-Tectonic Processes. Springer, Switzerland. https://doi.org/10.1007/978-3-030-65968-4.

Acocella, V., Neri, M., 2009. Dike propagation in volcanic edifices: Overview and possible developments. Tectonophysics 471 (1–2), 67–77. https://doi.org/10.1016/j.tecto.2008.10.002.

Acocella, V., Trippanera, D., 2016. How diking affects the tectonomagmatic evolution of slow spreading plate boundaries: Overview and model. Geosphere 12 (3), 867–883. https://doi.org/10.1130/ges01271.1.

Árnadóttir, T., Geirsson, H., Einarsson, P., 2004. Coseismic stress changes and crustal deformation on the Reykjanes Peninsula due to triggered earthquakes on 17 June 2000. J. Geophys. Res. Solid Earth 109 (B9). https://doi.org/10.1029/2004JB003130.

Barsotti, S., Parks, M.M., Pfeffer, M.A., Óladóttir, B.A., Barnie, T., Titos, M.M., Jónsdóttir, K., Pedersen, G.B., Hjartardóttir, Á.R., Stefansdóttir, G., 2023. The eruption in Fagradalsfjall (2021, Iceland): how the operational monitoring and the volcanic hazard assessment contributed to its safe access. Nat. Hazards 116 (3), 3063–3092. https://doi.org/10.1007/s11069-022-05798-7.

Beauducel, F., Carbone, D., 2015. A strategy to explore the topography-driven distortions in the tilt field induced by a spherical pressure source: the case of Mt Etna. Geophys. J. Int. 201 (3), 1471–1481. https://doi.org/10.1093/gji/ggv076.

Bonaccorso, A., Currenti, G., Del Negro, C., Boschi, E., 2010. Dike deflection modelling for inferring magma pressure and withdrawal, with application to Etna 2001 case. Earth Planet. Sci. Lett. 293 (1–2), 121–129. https://doi.org/10.1016/j.epsl.2010.02.030.

Bonali, F.L., Corti, N., Mariotto, F.P., De Beni, E., Bressan, S., Cantarero, M., Russo, E., Neri, M., Tibaldi, A., 2024. 3D study of dyke-induced asymmetric graben: the 1971 Mt. Etna (Italy) case by structural data and numerical modelling. J. Struct. Geol. 187, 105231. https://doi.org/10.1016/j.jsg.2024.105231.

Buck, W.R., Einarsson, P., Brandsdóttir, B., 2006. Tectonic stress and magma chamber size as controls on dike propagation: Constraints from the 1975–1984 Krafla rifting episode. J. Geophys. Res. Solid Earth 111 (B12). https://doi.org/10.1029/2005jb003879.

Bufféral, S., Panza, E., Mannini, S., Hjartardóttir, Á.R., Nobile, A., Gies, N., Óskarsson, B. V., Ruch, J., 2023. Surface fractures generated during the 2021 Reykjanes oblique rifting event (SW Iceland). Bull. Volcanol. 85 (11). https://doi.org/10.1007/s00445-023-01666-9.

Caracciolo, A., Bali, E., Halldórsson, S.A., Guðfinnsson, G.H., Kahl, M., Þórðardóttir, I., Pálmadóttir, G.L., Silvestri, V., 2023. Magma plumbing architectures and timescales of magmatic processes during historical magmatism on the Reykjanes Peninsula, Iceland. Earth Planet. Sci. Lett. 621. https://doi.org/10.1016/j.epsl.2023.118378.

Cayol, V., Cornet, F.H., 1998. Effects of topography on the interpretation of the deformation field of prominent volcanoes—Application to Etna. Geophys. Res. Lett. 25 (11), 1979–1982. https://doi.org/10.1029/98GL51512.

Clifton, A., Einarsson, P., 2005. Styles of surface rupture accompanying the June 17 and 21, 2000 earthquakes in the South Iceland Seismic Zone. Tectonophysics 396 (3–4), 141–159. https://doi.org/10.1016/j.tecto.2004.11.007.

Clifton, A.E., Kattenhorn, S.A., 2006. Structural architecture of a highly oblique divergent plate boundary segment. Tectonophysics 419 (1–4), 27–40. https://doi.org/10.1016/j.tecto.2006.03.016.

Clifton, A.E., Schlische, R.W., 2003. Fracture populations on the Reykjanes Peninsula, Iceland: Comparison with experimental clay models of oblique rifting. J. Geophys. Res. Solid Earth 108 (B2). https://doi.org/10.1029/2001jb000635.

Clifton, A.E., Schlische, R.W., Withjack, M.O., Ackermann, R.V., 2000. Influence of rift obliquity on fault-population systematics: results of experimental clay models. J. Struct. Geol. 22 (10), 1491–1509. https://doi.org/10.1016/S0191-8141(00)00043-2.

Clifton, A.E., Pagli, C., Jónsdóttir, J.F.s., Eythorsdóttir, K. and Vogfjörð, K., 2003. Surface effects of triggered fault slip on Reykjanes Peninsula. SW Iceland. Tectonophys. 369 (3–4), 145–154. https://doi.org/10.1016/s0040-1951(03)00201-4.

Dahm, T., 2000. Numerical simulations of the propagation path and the arrest of fluid-filled fractures in the Earth. Geophys. J. Int. 141 (3), 623–638. https://doi.org/10.1046/j.1365-246x.2000.00102.x.

Davis, T., Bagnardi, M., Lundgren, P., Rivalta, E., 2021. Extreme curvature of shallow magma pathways controlled by competing stresses: Insights from the 2018 Sierra Negra eruption. Geophys. Res. Lett. 48 (13). https://doi.org/10.1029/2021GL093038 e2021GL093038.

De Pascale, G.P., Fischer, T.J., Moreland, W.M., Geirsson, H., Hrubcová, P., Drouin, V., Forester, D., Payet Clerc, M., da Silveira, D.B., Vlček, J., Ófeigsson, B.G., Höskuldsson, Á., Torfadóttir, H.K., Valdimarsdóttir, I.K., Blöndal, B.D.J., Jónsdóttir, I., Jónsson, S., Thordarson, T., 2024. Geophys. Res. Lett. 51 (14). https://doi.org/10.1029/2024gl110150. On the Move: 2023 Observations on Real Time Graben Formation, Grindavík, Iceland.

DeMets, C., Gordon, R.G., Argus, D.F., 2010. Geologically current plate motions. Geophys. J. Int. 181 (1), 1–80. https://doi.org/10.1111/j.1365-246X.2009.04491.x.

Ducrocq, C., Árnadóttir, T., Einarsson, P., Jónsson, S., Drouin, V., Geirsson, H., Hjartardóttir, Á.R., 2024. Widespread fracture movements during a volcano-tectonic unrest: the Reykjanes Peninsula, Iceland, from 2019–2021 TerraSAR-X interferometry. Bull. Volcanol. 86 (2). https://doi.org/10.1007/s00445-023-01699-0.

Einarsson, P., 1991. Earthquakes and present-day tectonism in Iceland. Tectonophysics 189 (1–4), 261–279. https://doi.org/10.1016/0040-1951(91)90501-I.

Einarsson, P., 2008. Plate boundaries, rifts and transforms in Iceland. Doi:10.33799/jokull2008.58.035.

Einarsson, P., 2010. Mapping of Holocene surface ruptures in the South Iceland Seismic Zone. https://doi.org/10.33799/jokull2010.60.117.

Einarsson, P., Hjartardóttir, Á.R., Hreinsdóttir, S., Imsland, P., 2020. The structure of seismogenic strike-slip faults in the eastern part of the Reykjanes Peninsula Oblique Rift, SW Iceland. J. Volcanol. Geotherm. Res. 391, 106372. https://doi.org/10.1016/j.jvolgeores.2018.04.029.

Einarsson, P., Eyjólfsson, V., Hjartardóttir, Á.R., 2023. Tectonic framework and fault structures in the Fagradalsfjall segment of the Reykjanes Peninsula Oblique Rift, Iceland. Bull. Volcanol. 85 (2). https://doi.org/10.1007/s00445-022-01624-x.

Flóvenz, Ó.G., Wang, R., Hersir, G.P., Dahm, T., Hainzl, S., Vassileva, M., Drouin, V., Heimann, S., Isken, M.P., Gudnason, E.Á., 2022. Cyclical geothermal unrest as a precursor to Iceland's 2021 Fagradalsfjall eruption. Nat. Geosci. 15 (5), 397–404. https://doi.org/10.1038/s41561-022-00930-5.

Gaffney, E.S., Damjanac, B., 2006. Localization of volcanic activity: topographic effects on dike propagation, eruption and conduit formation. Geophys. Res. Lett. 33 (14). https://doi.org/10.1029/2006GL026852.

García-Pérez, T., Ferreira, A.M.G., Yáñez, G., Iturrieta, P., Cembrano, J., 2021. Effects of topography and basins on seismic wave amplification: the Northern Chile coastal cliff and intramountainous basins. Geophys. J. Int. 227 (2), 1143–1167. https://doi.org/10.1093/gji/ggab259.

Goldstein, R.M., Werner, C.L., 1998. Radar interferogram filtering for geophysical applications. Geophys. Res. Lett. 25 (21), 4035–4038. https://doi.org/10.1029/1998GL900033.

Greenfield, T., Winder, T., Rawlinson, N., Maclennan, J., White, R.S., Ágústsdóttir, T., Bacon, C.A., Brandsdóttir, B., Eibl, E.P., Glastonbury-Southern, E., 2022. Deep long period seismicity preceding and during the 2021 Fagradalsfjall Eruption. Iceland. Bull. Volcanol. 84 (12), 101. https://doi.org/10.1007/s00445-022-01603-2.

Gudmundsson, A., 1987. Geometry, formation and development of tectonic fractures on the Reykjanes Peninsula, Southwest Iceland. Tectonophysics 139 (3–4), 295–308. https://doi.org/10.1016/0040-1951(87)90103-X.

Hanssen, 2001. Radar Interferometry: Data Interpretation and Error Analysis.

Havenith, H.-B., Vanini, M., Jongmans, D., Faccioli, E., 2003. Initiation of earthquake-induced slope failure: influence of topographical and other site specific amplification effects. J. Seismol. 7, 397–412. https://doi.org/10.1023/A:1024534105559.

Hickey, J., Pascal, K., Syers, R., Alshembari, R., 2024. Topographical effects on volcano deformation signal intensity: Implications for GPS network configuration. Geophys. Res. Lett. 51 (12). https://doi.org/10.1029/2024GL108812 e2024GL108812.

Hjartardóttir, Á.R., Dürig, T., Parks, M., Drouin, V., Eyjólfsson, V., Reynolds, H., Einarsson, P., Jensen, E.H., Óskarsson, B.V., Belart, J.M.C., Ruch, J., Gies, N.B., Pedersen, G.B.M., 2023. Pre-existing fractures and eruptive vent openings during the 2021 Fagradalsfjall eruption, Iceland. Bull. Volcanol. 85 (10). https://doi.org/10.1007/s00445-023-01670-z.

Hurley, M., Oestreicher, N., Shevchenko, A.V., De Pascale, G.P., Gudmundsson, M.T., Gudnason, E.Á., Hersir, G.P., De Jarnatt, B.F., Joachim, A., Ruch, J., Bonali, F.L., Walter, T.R., 2025. Data Collection on Fractures, Sinkholes and Morphology of Mount Thorbjörn during the 2023–2024 Volcanic Unrest. GFZ Data Services, Iceland. https://doi.org/10.5880/GFZ.HDBG.2025.001.

IMO, 2024. The Second Largest Eruption at the Sundhnúkur Crater Row. Icelandic Meteorological Office.

James, M.R., Carr, B., D'Arcy, F., Diefenbach, A., Dietterich, H., Fornaciai, A., Lev, E., Liu, E., Pieri, D., Rodgers, M., 2020. Volcanological applications of unoccupied aircraft systems (UAS): Developments, strategies, and future challenges. Volcanica 3 (1), 67–114. https://doi.org/10.30909/vol.03.01.67114.

Jónsson, J., 1978. Geological map of the Reykjanes Peninsula. Orkustofnun, report OS-JHD 7831, 332.

Keiding, M., Lund, B., Árnadóttir, T., 2009. Earthquakes, stress, and strain along an obliquely divergent plate boundary: Reykjanes Peninsula, Southwest Iceland. J. Geophys. Res. Solid Earth 114 (B9). https://doi.org/10.1029/2008JB006253.

Kervyn, M., Ernst, G.G.J., van Wyk de Vries, B., Mathieu, L., Jacobs, P., 2009. Volcano load control on dyke propagation and vent distribution: Insights from analogue modeling. J. Geophys. Res. Solid Earth 114 (B3). https://doi.org/10.1029/2008jb005653.

Khodayar, M., Einarsson, P., 2002. Strike-slip faulting, normal faulting, and lateral dike injections along a single fault: Field example of the Gljúfurá fault near a Tertiary oblique rift-transform zone, Borgarfjörður, West Iceland. J. Geophys. Res. Solid Earth 107 (B5). https://doi.org/10.1029/2001JB000150. ETG 5-1-ETG 5-16.

Koons, P.O., Kirby, E., 2007. Topography, Denudation, and Deformation: The Role of Surface Processes in Fault Evolution. https://doi.org/10.7551/mitpress/6703.001.0001.

Le Corvec, N., Walter, T.R., 2009. Volcano spreading and fault interaction influenced by rift zone intrusions: Insights from analogue experiments analyzed with digital image correlation technique. J. Volcanol. Geotherm. Res. 183 (3–4), 170–182. https://doi.org/10.1016/j.jvolgeores.2009.02.006.

Le Corvec, N., Menand, T., Lindsay, J., 2013. Interaction of ascending magma with pre-existing crustal fractures in monogenetic basaltic volcanism: an experimental approach. J. Geophys. Res. Solid Earth 118 (3), 968–984. https://doi.org/10.1002/jgrb.50142.

Lewicka, O., Specht, M., Specht, C., 2022. Assessment of the Steering Precision of a UAV along the Flight Profiles using a GNSS RTK Receiver. Remote Sens. 14 (23), 6127. https://doi.org/10.3390/rs14236127.

Maccaferri, F., Rivalta, E., Keir, D., Acocella, V., 2014. Off-rift volcanism in rift zones determined by crustal unloading. Nat. Geosci. 7 (4), 297–300. https://doi.org/10.1038/NGEO2110.

Maccaferri, F., Richter, N., Walter, T.R., 2017. The effect of giant lateral collapses on magma pathways and the location of volcanism. Nat. Commun. 8 (1), 1097. https://doi.org/10.1038/s41467-017-01256-2.

Massa, M., Lovati, S., D'Alema, E., Ferretti, G., Bakavoli, M., 2010. An Experimental Approach for estimating Seismic Amplification Effects at the top of a Ridge, and the Implication for Ground-Motion predictions: the Case of Narni, Central Italy. Bull. Seismol. Soc. Am. 100 (6), 3020–3034. https://doi.org/10.1785/0120090382.

Mastin, L.G., Pollard, D.D., 1988. Surface deformation and shallow dike intrusion processes at Inyo Craters, Long Valley, California. J. Geophys. Res. Solid Earth 93 (B11), 13221–13235. https://doi.org/10.1029/JB093iB11p13221.

McGuire, W. and Pullen, A., 1989. Location and orientation of eruptive fissures and feederdykes at Mount Etna; influence of gravitational and regional tectonic stress regimes. J. Volcanol. Geotherm. Res., 38(3–4): 325–344. doi:https://doi.org/10.1016/0377-0273(89)90046-2.

McNutt, M., 1980. Implications of regional gravity for state of stress in the Earth's crust and upper mantle. J. Geophys. Res. Solid Earth 85 (B11), 6377–6396. https://doi.org/10.1029/JB085iB11p06377.

McTigue, D.F., Mei, C.C., 1981. Gravity-induced stresses near topography of small slope. J. Geophys. Res. Solid Earth 86 (B10), 9268–9278. https://doi.org/10.1029/JB086iB10p09268.

Miller, D.J., Dunne, T., 1996. Topographic perturbations of regional stresses and consequent bedrock fracturing. J. Geophys. Res. Solid Earth 101 (B11), 25523–25536. https://doi.org/10.1029/96jb02531.

Molnar, P., Anderson, R.S., Anderson, S.P., 2007. Tectonics, fracturing of rock, and erosion. J. Geophys. Res. Earth 112 (F3). https://doi.org/10.1029/2005jf000433.
Muller, J.R., Ito, G., Martel, S.J., 2001. Effects of volcano loading on dike propagation in an elastic half-space. J. Geophys. Res. Solid Earth 106 (B6), 11101–11113. https://doi.org/10.1029/2000JB900461.
Müller, D., Walter, T.R., Schöpa, A., Witt, T., Steinke, B., Gudmundsson, M.T., Dürig, T., 2017. High-Resolution Digital Elevation Modeling from TLS and UAV Campaign reveals Structural Complexity at the 2014/2015 Holuhraun Eruption Site, Iceland. Front. Earth Sci. 5. https://doi.org/10.3389/feart.2017.00059.
Pan, B., Qian, K., Xie, H., Asundi, A., 2009. Two-dimensional digital image correlation for in-plane displacement and strain measurement: a review. Meas. Sci. Technol. 20 (6). https://doi.org/10.1088/0957-0233/20/6/062001.
Panza, E., Ruch, J., Oestreicher, N., 2024. Rift obliquity in the Northern Volcanic Zone in Iceland using UAV-based structural data. J. Volcanol. Geotherm. Res. 450. https://doi.org/10.1016/j.jvolgeores.2024.108072.
Pedersen, G., Grosse, P., 2014. Morphometry of subaerial shield volcanoes and glaciovolcanoes from Reykjanes Peninsula, Iceland: effects of eruption environment. J. Volcanol. Geotherm. Res. 282, 115–133. https://doi.org/10.1016/j.jvolgeores.2014.06.008.
Pedersen, G.B., Grosse, P., Gudmundsson, M.T., 2020. Morphometry of glaciovolcanic edifices from Iceland: Types and evolution. Geomorphology 370, 107334. https://doi.org/10.1016/j.geomorph.2020.107334.
Pinel, V., Jaupart, C., 2000. The effect of edifice load on magma ascent beneath a volcano. Philos. Trans. R. Soc. London, Ser. A 358 (1770), 1515–1532. https://doi.org/10.1098/rsta.2000.0601.
Pinel, V., Jaupart, C., 2004a. Likelihood of basaltic eruptions as a function of volatile content and volcanic edifice size. J. Volcanol. Geotherm. Res. 137 (1–3), 201–217. https://doi.org/10.1016/j.jvolgeores.2004.05.010.
Pinel, V., Jaupart, C., 2004b. Magma storage and horizontal dyke injection beneath a volcanic edifice. Earth Planet. Sci. Lett. 221 (1–4), 245–262.
Pollard, D.D., Delaney, P.T., Duffield, W.A., Endo, E.T., Okamura, A.T., 1983. Surface deformation in volcanic rift zones. Develop. Geotect. Elsevier 541–584. https://doi.org/10.1016/B978-0-444-42198-2.50036-5.
Ricard, Y., Fleitout, L., Froidevaux, C., 1984. Geoid heights and lithospheric stresses for a dynamic Earth. Ann. Geophys. 267–286.
Rivalta, E., Corbi, F., Passarelli, L., Acocella, V., Davis, T., Di Vito, M.A., 2019. Stress inversions to forecast magma pathways and eruptive vent location. Sci. Adv. 5 (7), eaau9784. https://doi.org/10.1126/sciadv.aau9784.
Rubin, A.M., Pollard, D.D., 1988. Dike-induced faulting in rift zones of Iceland and Afar. Geology 16 (5), 413–417. https://doi.org/10.1130/0091-7613(1988)016<0413:DIFIRZ>2.3.CO;2.
Ruch, J., Wang, T., Xu, W., Hensch, M., Jonsson, S., 2016. Oblique rift opening revealed by reoccurring magma injection in Central Iceland. Nat. Commun. 7, 12352. https://doi.org/10.1038/ncomms12352.
Russell, J., Edwards, B.R., Porritt, L., Ryane, C., 2014. Tuyas: a descriptive genetic classification. Quat. Sci. Rev. 87, 70–81. https://doi.org/10.1016/j.quascirev.2014.01.001.
Sæmundsson, K., Jóhannesson, H., Hjartarson, Á., Kristinsson, S.G., Sigurgeirsson, M., 2016. Geological Map of Southwest Iceland, 1: 100000 (Iceland geosurvey).
Sæmundsson, K., Sigurgeirsson, M.Á., Friðleifsson, G.Ó., 2020. Geology and structure of the Reykjanes volcanic system, Iceland. J. Volcanol. Geotherm. Res. 391, 106501. https://doi.org/10.1016/j.jvolgeores.2018.11.022.
Scott, C., Bunds, M., Shirzaei, M., Toke, N., 2020. Creep along the Central San Andreas Fault from surface fractures, topographic differencing, and InSAR. Journal of Geophysical Research: Solid. Earth 125 (10). https://doi.org/10.1029/2020JB019762 e2020JB019762.
Segall, P., 2010. Earthquake and Volcano Deformation. Princeton University Press, Earthquake and volcano deformation.
Shevchenko, A.V., Walter, T.R., Dvigalo, V.N., 2021. Morphology of Mount Thorbjorn, Iceland, Studied with UAS Photogrammetry. IEEE Int. Geosci. Remote Sens. Sympos. IGARSS 2021, 6607–6609. https://doi.org/10.1109/igarss47720.2021.9554243.
Sigmundsson, F., 2006. Crustal Deformation and Divergent Plate Tectonics. Berlin. https://doi.org/10.1007/3-540-37666-6.
Sigmundsson, F., Hooper, A., Hreinsdottir, S., Vogfjord, K.S., Ofeigsson, B.G., Heimisson, E.R., Dumont, S., Parks, M., Spaans, K., Gudmundsson, G.B., Drouin, V., Arnadottir, T., Jonsdottir, K., Gudmundsson, M.T., Hognadottir, T., Fridriksdottir, H. M., Hensch, M., Einarsson, P., Magnusson, E., Samsonov, S., Brandsdottir, B., White, R.S., Agustsdottir, T., Greenfield, T., Green, R.G., Hjartardottir, A.R., Pedersen, R., Bennett, R.A., Geirsson, H., La Femina, P.C., Bjornsson, H., Palsson, F., Sturkell, E., Bean, C.J., Mollhoff, M., Braiden, A.K., Eibl, E.P., 2015. Segmented lateral dyke growth in a rifting event at Baretharbunga volcanic system. Iceland. Nature 517 (7533), 191–195. https://doi.org/10.1038/nature14111.
Sigmundsson, F., Einarsson, P., Hjartardóttir, Á.R., Drouin, V., Jónsdóttir, K., Arnadottir, T., Geirsson, H., Hreinsdottir, S., Li, S., Ofeigsson, B.G., 2020. Geodynamics of Iceland and the signatures of plate spreading. J. Volcanol. Geotherm. Res. 391, 106436. https://doi.org/10.1016/j.jvolgeores.2018.08.014.
Sigmundsson, F., Parks, M., Geirsson, H., Hooper, A., Drouin, V., Vogfjord, K.S., Ofeigsson, B.G., Greiner, S.H.M., Yang, Y., Lanzi, C., De Pascale, G.P., Jonsdottir, K., Hreinsdottir, S., Tolpekin, V., Friethriksdottir, H.M., Einarsson, P., Barsotti, S., 2024. Fracturing and tectonic stress drive ultrarapid magma flow into dikes. Science 383 (6688), 1228–1235. https://doi.org/10.1126/science.adn2838.
Steigenberger, P., Seitz, M., Böckmann, S., Tesmer, V., Hugentobler, U., 2012. Precision and accuracy of GPS-derived station displacements. Physics and Chemistry of the Earth, Parts A/B/C 53, 72–79. https://doi.org/10.1016/j.pce.2010.07.035.
Tibaldi, A., 1998. Effects of topography on surface fault geometry and kinematics: examples from the Alps, Italy and Tien Shan, Kazakstan. Geomorphology 24 (2–3), 225–243. https://doi.org/10.1016/S0169-555X(98)00018-X.
Tibaldi, A., 2015. Structure of volcano plumbing systems: a review of multi-parametric effects. J. Volcanol. Geotherm. Res. 298, 85–135. https://doi.org/10.1016/j.jvolgeores.2015.03.023.
Tibaldi, A., Bonali, F.L., Corti, N., Russo, E., Drymoni, K., De Beni, E., Branca, S., Neri, M., Cantarero, M., Mariotto, F.P., 2022. Surface deformation during the 1928 fissure eruption of Mt. Etna (Italy): Insights from field data and FEM numerical modelling. Tectonophysics 837. https://doi.org/10.1016/j.tecto.2022.229468.
Trippanera, D., Ruch, J., Acocella, V., Rivalta, E., 2015. Experiments of dike-induced deformation: Insights on the long-term evolution of divergent plate boundaries. J. Geophys. Res. Solid Earth 120 (10), 6913–6942. https://doi.org/10.1002/2014jb011850.
Trippanera, D., Ruch, J., Passone, L., Jónsson, S., 2019. Structural Mapping of Dike-Induced Faulting in Harrat Lunayyir (Saudi Arabia) by using High Resolution Drone Imagery. Front. Earth Sci. 7. https://doi.org/10.3389/feart.2019.00168.
Troll, V.R., Deegan, F.M., Thordarson, T., Tryggvason, A., Krmíček, L., Moreland, W.M., Lund, B., Bindeman, I.N., Höskuldsson, Á., Day, J.M., 2024. The Fagradalsfjall and Sundhnúkur fires of 2021–2024: a single magma reservoir under the Reykjanes Peninsula, Iceland? Terra Nova 36 (6), 447–456. https://doi.org/10.1111/ter.12733.
Upton, P., Song, B.R., Koons, P.O., 2017. Topographic control on shallow fault structure and strain partitioning near Whataroa, New Zealand demonstrates weak Alpine Fault. N. Z. J. Geol. Geophys. 61 (1), 1–8. https://doi.org/10.1080/00288306.2017.1397706.
Walker, G.P., 1995. Flood basalts versus central volcanoes and the British Tertiary Volcanic Province. Geol. Soc. Lond. Mem. 16 (1), 195–202. https://doi.org/10.1144/GSL.MEM.1995.016.01.20.
Walter, T.R., 2011. Low cost volcano deformation monitoring: optical strain measurement and application to Mount St. Helens data. Geophys. J. Int. 186 (2), 699–705. https://doi.org/10.1111/j.1365-246X.2011.05051.x.
Walter, T.R., Zorn, E.U., González, P.J., Sansosti, E., Muñoz, V., Shevchenko, A.V., Plank, S.M., Reale, D., Richter, N., 2023. Late complex tensile fracturing interacts with topography at Cumbre Vieja. La Palma. https://doi.org/10.30909/vol.06.01.0117.
Watanabe, T., Masuyama, T., Nagaoka, K., Tahara, T., 2002. Analog experiments on magma-filled cracks: competition between external stresses and internal pressure. Earth Planets Space 54 (12), 1247–1261. https://doi.org/10.1186/BF03352453.
Wesnousky, S.G., 2005. The San Andreas and Walker Lane fault systems, western North America: Transpression, transtension, cumulative slip and the structural evolution of a major transform plate boundary. J. Struct. Geol. 27 (8), 1505–1512. https://doi.org/10.1016/j.jsg.2005.01.015.
Wessel, B., Huber, M., Wohlfart, C., Marschalk, U., Kosmann, D., Roth, A., 2018. Accuracy assessment of the global TanDEM-X Digital Elevation Model with GPS data. ISPRS J. Photogramm. Remote Sens. 139, 171–182. https://doi.org/10.1016/j.isprsjprs.2018.02.017.
Westoby, M.J., Brasington, J., Glasser, N.F., Hambrey, M.J., Reynolds, J.M., 2012. Structure-from-Motion'photogrammetry: a low-cost, effective tool for geoscience applications. Geomorphology 179, 300–314. https://doi.org/10.1016/j.geomorph.2012.08.021.
Williams, R., 2012. DEMs of difference. Geomorphological. Techniques 2 (3.2).
Williams, C.A., Wadge, G., 1998. The effects of topography on magma chamber deformation models: Application to Mt. Etna and radar interferometry. Geophys. Res. Lett. 25 (10), 1549–1552. https://doi.org/10.1029/98GL01136.
Williams, C.A., Wadge, G., 2000. An accurate and efficient method for including the effects of topography in three-dimensional elastic models of ground deformation with applications to radar interferometry. J. Geophys. Res. Solid Earth 105 (B4), 8103–8120. https://doi.org/10.1029/1999JB900307.
Wooller, L., van Wyk de Vries, B., Cecchi, E. and Rymer, H., 2009. Analogue models of the effect of long-term basement fault movement on volcanic edifices. Bull. Volcanol. 71 (10), 1111–1131. https://doi.org/10.1007/s00445-009-0289-3.
Wright, T.J., Ebinger, C., Biggs, J., Ayele, A., Yirgu, G., Keir, D., Stork, A., 2006. Magma-maintained rift segmentation at continental rupture in the 2005 Afar dyking episode. Nature 442 (7100), 291–294. https://doi.org/10.1038/nature04978.
Yan, H., Dai, W., Xu, W., Shi, Q., Sun, K., Lu, Z., Wang, R., 2024. A method for correcting InSAR interferogram errors using GNSS data and the K-means algorithm. Earth Planets Space 76 (1), 51. https://doi.org/10.1186/s40623-024-01999-5.
Ziegler, M., Loew, S., Amann, F., 2016. Near-surface rock stress orientations in alpine topography derived from exfoliation fracture surface markings and 3D numerical modelling. Int. J. Rock Mech. Min. Sci. 85, 129–151. https://doi.org/10.1016/j.ijrmms.2016.03.009.
Zorn, E.U., Walter, T.R., Johnson, J.B., Mania, R., 2020. UAS-based tracking of the Santiaguito Lava Dome. Guatemala. Sci Rep 10 (1), 8644. https://doi.org/10.1038/s41598-020-65386-2.